Electro-optic beam steering using Domain Engineered Lithium Tantalate

THESIS

Daren J. Chauvin, Captain, USAF

AFIT/GEO/ENP/05-01

DEPARTMENT OF THE AIR FORCE
AIR UNIVERSITY

AIR FORCE INSTITUTE OF TECHNOLOGY

Wright-Patterson Air Force Base, Ohio

APPROVED FOR PUBLIC RELEASE; DISTRIBUTION UNLIMITED.

The view expressed in this thesis are those of the author and do not reflect the official policy or position of the United States Air Force, Department of Defense, or the United States Government.

AFIT/GEO/ENP/05-01

Electro-optic beam steering using Domain Engineered Lithium Tantalate

THESIS

Presented to the Faculty

Department of Engineering Physics

Graduate School of Engineering and Management

Air Force Institute of Technology

Air University

Air Education and Training Command

In Partial Fulfillment of the Requirements for the

Degree of Master of Science in Electrical Engineering

Daren J. Chauvin, B.S.E.E.

Captain, USAF

March 2005

APPROVED FOR PUBLIC RELEASE; DISTRIBUTION UNLIMITED.

AFIT/GEO/ENP/05-01

Electro-optic beam steering using Domain Engineered Lithium Tantalate

Daren J. Chauvin, B.S.E.E.
Captain, USAF

Approved:

/signed/	21 Mar 2005
Thomas G. Alley (Chairman)	date
/signed/	21 Mar 2005
Won B. Roh (Member)	date
/signed/	21 Mar 2005
Kenneth L. Schepler (Member)	date

AFIT/GEO/ENP/05-01

Abstract

This research studied the operation of a 14-channel five stage electro-optic beam steering device. Device operation demonstrated a beam deflection scanned through a range from 0° to 10.1°. The maximum angle is within 0.3% of the designed angle. Many laser systems in operation today implement mechanical beam steering methods that are often expensive in terms of cost, weight and power. They are slow and subject to wear and vibration. A non-inertial beam scanning mechanism, such as one based on the device studied in this research could enhance the performance of these systems. The 14-channel, five-stage device studied here is fabricated in LiTaO3 using micro-patterned domain reversal. The 14 channels allow for steering large aperture beams while the five cascaded stages increase the total deflection angle. The steering mechanism is a series of prisms created through domain reversal and the index change across prism interfaces is controlled electro-optically. The voltage applied to each stage for maximum deflection was 1.43 kV. The maximum coupling efficiency achieved was 61.6% for this device. Also, the far-field observations revealed a pattern consistent with a beam diffracted through a many slit aperture. There are 'forbidden angles' between modes which do not receive constructive interference regardless of the applied voltage. A discussion on a method to improve device design, which allows the forbidden angles, is presented.

Acknowledgements

First and foremost I humbly offer thanks and praise to my Lord, Christ Jesus. His wisdom and strength has sustained me through this difficult effort. I extend my gratitude and respect to my wife, Dawn, for her self-sacrifice, for all she has tolerated from me and all that she has had to do for me and our children during our time in this program. Thanks also to my children for patiently enduring the countless times when research or course work prevented me from fulfill my fatherly duties.

I would like to thank my thesis adviser, Lt Col Thomas Alley for his guidance, wisdom, and continually encouraging me. I also appreciate the support from everyone at my sponsoring organization (AFRL/SNJW). Specifically, I thank Dr Ken Schepler for providing me the equipment and lab space to perform the experiments. Additionally, he and Dr Rita Peterson always provided advice and guidance whenever I needed it. Thanks to Mr. John McCurdy for his help and expertise in building the power supplies for driving my experimental devices. I thank Mr. Eric Vershure for his help in the device fabrication efforts and Lt Mike Plourde for LabVIEW development assistance. I also thank Mr Dave Mohler for designing and building the device mount. Finally I wish to thank Dr Venkat Gopalan of Penn State University for the initial guidance on this experiment. He also provided the fabricated devices used in this experiment.

Daren J. Chauvin

Table of Contents

Page

List of Figures

List of Tables

Electro-optic beam steering using Domain Engineered Lithium Tantalate

I. Introduction

There is a wide and growing range of uses for laser systems in military applications. This includes communication systems such as free space interconnections, imaging and ranging systems and countermeasure systems. Many of these applications require precise beam control. A variety of beam steering techniques are well known utilizing numerous electro-mechanical, acousto-optic and electro-optic steering mechanisms [3, 7, 14, 15, 17, 18].

As a special motivation for this research effort, the Air Force recognizes a continuing threat from infrared guided weapon systems. Optical beam countermeasures utilizing infrared laser systems are of great importance. Most current beam steering applications, including infrared countermeasure systems, use mechanical means such as motorized gimbals for beam deflection. Mechanical steering systems are often expensive in terms of cost, weight and power. They are slow and subject to wear and vibration. Development of a robust non-inertial laser scanning device could enhance the performance of these systems. A non-inertial system, such as an electro-optic device, which can be implemented with readily available crystalline materials and fabricated using familiar techniques, promises faster scanning, lower production and maintenance costs, and higher reliability.

Electro-optic beam steering is achieved by modulating the refractive indices of a material with an applied electric field. The refraction angle of a beam crossing an electro-optically modulated interface, or series of interfaces, is therefore controlled by the applied electric field. Several specific techniques for implementing electro-optic beam steering have been reported, most of which fall into one of the following three types: grazing angle, gradient and prism scanners. In grazing angle scanners as shown

in Figure 1.1(a) [6], the angle of the optical beam impinging on an electro-optically controlled interface approaches the total internal reflection (TIR) limit angle. A scanner of this type has been shown to have a deflection angle that is a function of the applied voltage and the incident angle [6]. In gradient scanners like in Figure 1.1(b) [5], a nonuniform electric field distribution is created in the crystal. The nonuniform field induces an index distribution which bends the light as it propagates through the device. In prism scanners like Figure 1.1(c) [5], an applied electric field causes the indicated changes in the refractive indices of the triangular prism-shaped regions via the electro-optic effect. The prism regions can be defined by arranging a number of crystals in opposite orientations [11], or by inverting ferroelectric domains in a single substrate [4]. The amount of deflection caused at each interface is controlled by the applied electric field. The total deflection can be found by applying Snell′s law at each interface. The electro-optic effect and the development of the total deflection angle for a prism scanner is covered in Chapter II.

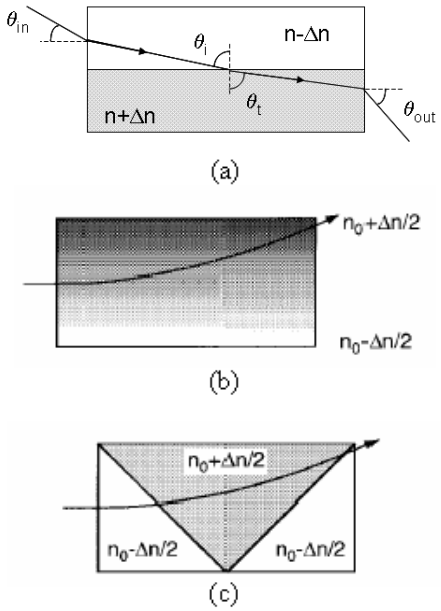

Figure 1.1: (a) Grazing angle electro-optic beam scanner,(b) Gradient type electro-optic beam scanner, (c)Prism type electro-optic beam scanner.

Additional attempts to improve upon the basic prism scanning designs have been made. A horn-shaped prism scanner design [17] and cascaded prism scanning sections [18] have been demonstrated to achieve deflection angles at 10°-15° and greater in one dimension. A method for two-dimensional beam steering using a design similar to the grazing angle geometry of Figure 1.1(a) was shown to reach an angle of approximately 3° [1]. Therefore the larger deflection angle of prism scanners may prove advantageous.

The device studied in this research is an electro-optic prism deflector based on domain inverted ferroelectric crystals. There are considerations that generally limit the beam size that can be deflected at reasonable angles by these devices. First, the deflection angle is directly related to the strength of the electric field polarized normal to the plane of the device. As the thickness of the device increases so must the level of the voltage across the device to achieve given electric field strength. A tradeoff arises between device thickness required for larger beams and higher voltage required for a given deflection angle. Second, in the plane of the device, the deflection angle is inversely related to the width of the domain prisms, as will be further explained in Chapter II. This results in a tradeoff between beam size in the plane of the device and deflection angle.

This research is a continuation of work previously reported on a 14-channel, five-stage electro-optic beam scanner [19] in domain engineered $LiTaO_3$. The device studied here implements wide aperture beam steering in the plane of the device by splitting the beam into smaller beamlets that are scanned separately by an array of individual prism scanners as shown in Figure 1.2 [19].

The goal of this research is to advance the capability to steer large diameter beams with a large deflection angle. This thesis investigated the operating characteristics of the device under study. Chapter II of this thesis covers the theory needed for understanding the design and operation of the device. Chapter III is a brief description of the device fabrication process. Chapter IV presents the details of the

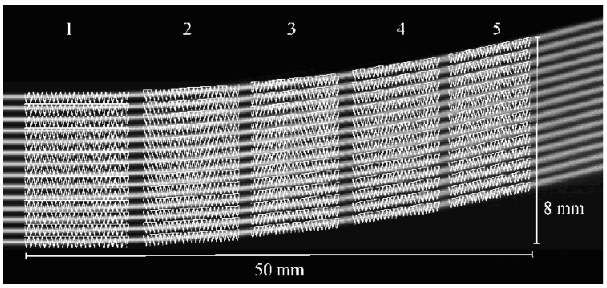

Figure 1.2: Beam propagation model simulation of 5-stage 14-beamlet scanner showing full deflection.

experiments conducted. This is followed by a presentation of the experimental results in Chapter V. Finally, the conclusions are presented in Chapter VI.

II. Theory

2.1 Introduction

This chapter covers the essential concepts necessary for understanding the operation of the device under study. First is a discussion of design principles affecting the device geometry. Second is a brief treatment of domain poling in ferroelectric material. Next, a development of the relationship between the refractive index of an anisotropic medium and the polarization of the propagating light is presented. This leads to the presentation of the electro-optic effect and the change of index induced by an applied electric field at the domain interface of a poled ferroelectric as in our device.

2.2 Beam Deflection

The prism is a simple geometry for deflecting light. A series of prisms can be used to increase the deflection angle. Each prism in the series deflects the light beam further and further from the original path. However, the total deflection angle should be small enough so the beam path remains contained within the prism width through the length of the series.

To determine the total deflection for a rectangular prism scanner [11, 17], one starts with Snell's Law at a single interface as seen in Figure 2.1 [5]. Snell's Law for this interface can be expressed as

$$\left(n_0 + \frac{\Delta n}{2}\right) sin\,(\alpha - \theta) = \left(n_0 - \frac{\Delta n}{2}\right) sin\,(\alpha) \tag{2.1}$$

where n_0 is the refractive index of the crystal when no electric field is present, Δn is the total electro-optically induced change in the refractive index across the interface, α is the angle of incidence at the interface and θ is the angle of deflection. Notice in Figure 2.1 that the change in index on one side of the interface is $-\frac{\Delta n}{2}$ and $\frac{\Delta n}{2}$ on the other. The equal but opposite changes results in a total index change across the interface of Δn. See the section on anisotropic medium, and specifically the subsection

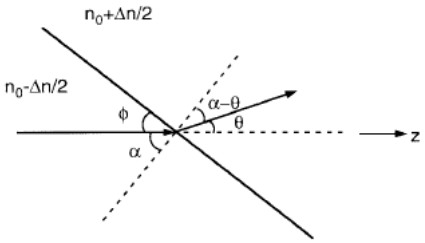

Figure 2.1: Beam deflection at a single interface.

on the electro-optic effect, in this chapter for a development of the induced change in the index of refraction.

Using the following trigonometric difference angle identity

$$\sin(\alpha - \theta) = \sin(\alpha)\cos(\theta) - \cos(\alpha)\sin(\theta) \tag{2.2}$$

Equation 2.1 can be written

$$\left(n_0 + \frac{\Delta n}{2}\right)[\sin(\alpha)\cos(\theta) - \sin(\theta)\cos(\alpha)] = \left(n_0 - \frac{\Delta n}{2}\right) sin(\alpha)\,. \tag{2.3}$$

When θ is small $\sin(\theta) \approx \theta$ and $\cos(\theta) \approx 1$. Equation 2.3 becomes

$$\left(n_0 + \frac{\Delta n}{2}\right)[\sin(\alpha) - \theta\cos(\alpha)] \approx \left(n_0 - \frac{\Delta n}{2}\right)\sin(\alpha) \tag{2.4}$$

or, when the $\sin(\alpha)$ terms are combined

$$\left(n_0 + \frac{\Delta n}{2}\right)\theta\cos(\alpha) \approx \Delta n \sin(\alpha)\,. \tag{2.5}$$

Finally, if $\Delta n \ll n_0$, solving for θ yields the following approximation

$$\theta \approx \frac{\Delta n}{n}\tan(\alpha) = \frac{\Delta n}{n}\tan(\frac{\pi}{2} - \phi) = \frac{\Delta n}{n}\cot(\phi) = \frac{\Delta n}{n}\frac{l}{W} \tag{2.6}$$

where ϕ is the angle between the interface and the incident ray, l is the length of the dielectric segment along the z-axis and W is the width of the scanner. For multiple

interfaces the combined deflection angle is found by summing the deflection at each interface. For a multiple-prism scanner as shown in Figure 2.2 the total internal deflection angle, θ_{int}, is thus

$$\theta_{int} = \frac{\Delta n}{n}\frac{l_1}{W} + \frac{\Delta n}{n}\frac{l_2}{W} + ... + \frac{\Delta n}{n}\frac{l_i}{W} \tag{2.7}$$

where l_1, l_2, ... l_i are the lengths of each segmented interface. When L is taken to be the sum of all the segmented lengths, Equation 2.7 can be simplified as

$$\theta_{int} = \frac{\Delta n}{n}\frac{L}{W}. \tag{2.8}$$

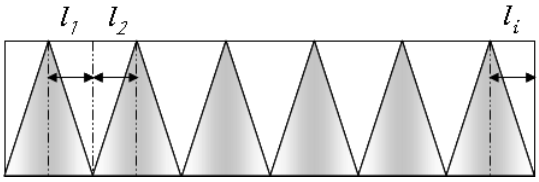

Figure 2.2: Rectangular prism scanner.

The equation above shows that with a greater length, L, and a narrower width, W, a higher deflection angle, θ, can be achieved. This equation reveals the trade-off in scanner design. Although W should be small to maximize θ, it must be large enough to contain the deflected beam at the output. If W is made too small or L is made too large, the beam will not be confined within the device as seen in Figure 2.3.

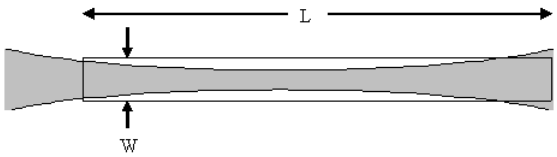

Figure 2.3: Here is an illustration of a beam that becomes too large to remain confined in the channel because of beam expansion, even without deflection. The width must be increased or the the length decreased. When deflection is included the width and length requirements become even more restricted.

The angle in Equations 2.7 and 2.8 is called the internal angle because the scanning device studied was fabricated in a ferroelectric medium and when the beam exists in this medium there is an additional deflection at the external interface with air. The total deflection including the additional external deflection can, from Snell's law, be written as

$$\theta_{ext} = \sin^{-1}\left[n \sin\left(\theta_{int}\right)\right] \tag{2.9}$$

The horn-shaped scanner as seen in the simulation in Figure 2.4 [5] has been proposed to maximize the steering angle. While the rectangular prism scanner must be wide enough to contain the beam through its diverging beam path, the horn-shape design allows the width of the scanner to be small at the device entrance. The width of the scanner grows down the length of the device to accommodate the diverging path of the beam. This keeps W as small as possible at every point along the path maximizing the possible deflection angle. Steering angles as high as 14.88° for a device with the entrance width, W_1, of 250 mm, the exit width, W_2, of 1500 mm and a length, L, of 15 mm have been reported [17]. This performance has been improved upon by adding multiple stages to the horn-shaped device. Figure 2.5 shows a BPM simulation of a two-stage horn-shaped scanner that achieved 26.08° [18].

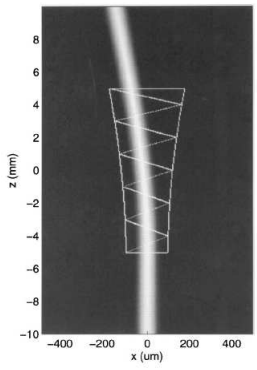

Figure 2.4: Horn-shaped prism scanner.

However, the horn shape does not have the same benefit for some large aperture beam applications. The horn shape increases beam deflection by eliminating uniform device width, reducing the width as much as possible. Large aperture beams require a

large width just to accommodate the beam itself, not just its deflection path. Focusing the beam to smaller size has limitations. For example, a beam focused to a smaller spot size will expand faster and therefore L would have to be shortened which would offset the deflection gained by narrowing W. Also, focusing a high power beam could damage the scanning device. The device studied in this research implements a design with multiple channels to contain a large beam which has been spilt into a set of beamlets. Although, the multi-channel design used in the current device is incompatible with the standard bi-directional horn shape in Figure 2.5, it still makes use of the shape optimizing design principles of the horn shaped scanner discussed here and detailed more fully elsewhere [5, 17].

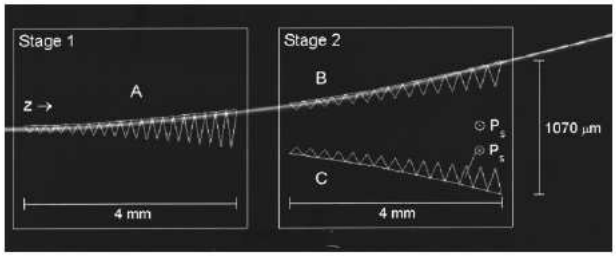

Figure 2.5: Two-stage horn-shaped prism scanner.

The current design is a modified form of the standard horn-shaped scanner design. As seen in the device structure in Figure 2.6 generated from the device design code provided by the Materials Research Institute at Penn State University (PSU), the device is designed to steer in one direction only. The channels of the device provide a path that follows a slowly sloping horn shape, but only toward one side. The width, W, is therefore kept small for each individual beamlet path. The standard horn-shape could not be used for the multi-channel design without each channel overlapping adjacent channels.

To increase the deflection angle range, a separate integrated device could be added in series to steer in the opposite direction. Also, it might be possible to provide steering for a two-dimensional array of beamlets by stacking devices. However, for this research a single device was used to characterize steering in one direction for a

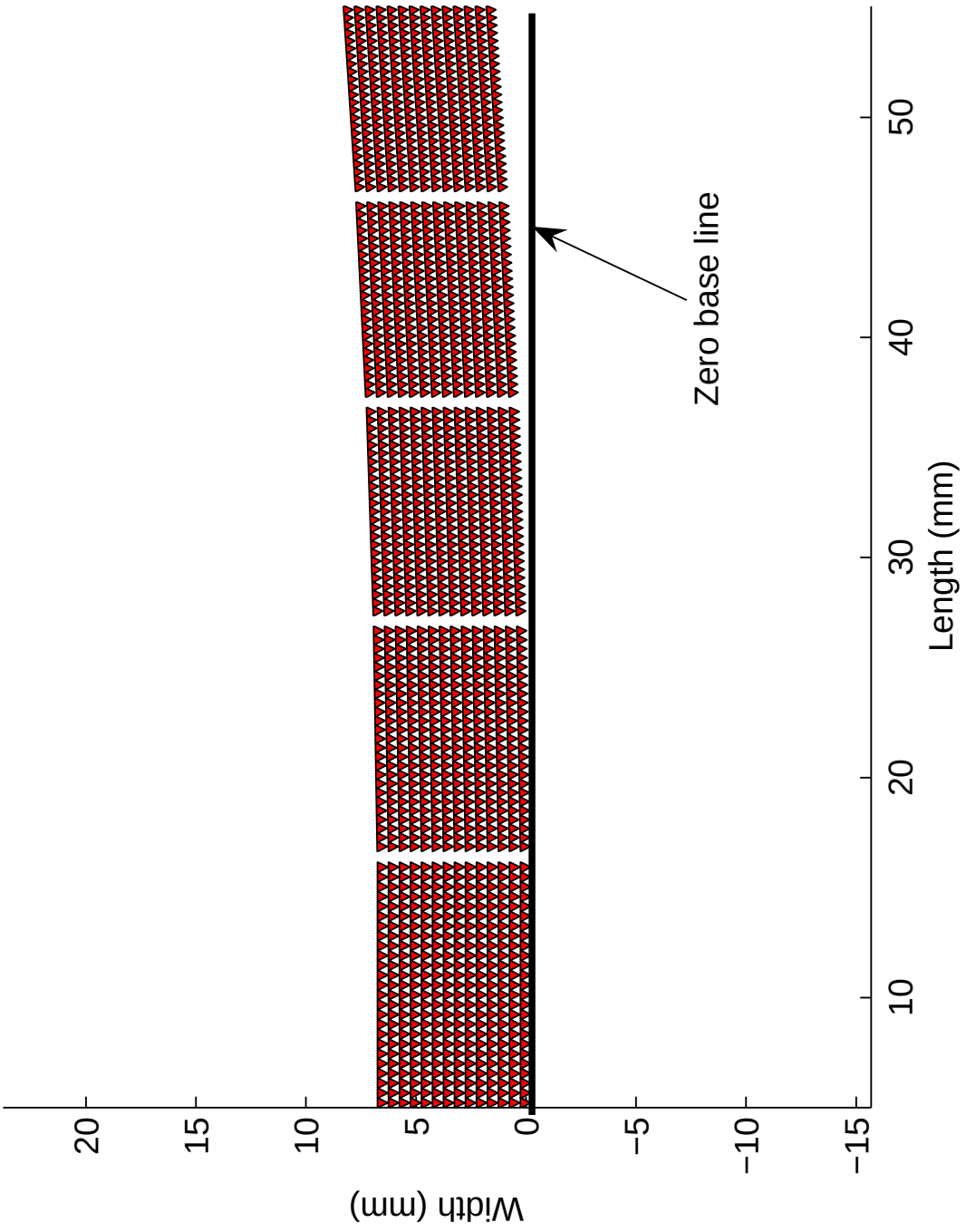

Figure 2.6: 5-stage device structure generated from Matlab code. The zero base line shows the device tilts away from the parallel path increasingly with each stage.

single row of beamlets. For more information on this, see the experimental set up in Chapter IV.

2.3 Ferroelectric Domain Engineering

This section gives a brief introduction to the concept of ferroelectric domain inversion by poling. It is not intended to give a detailed description of the laboratory techniques for this process. That topic is treated more fully in Chapter III.

A limited set of crystal point groups possess a permanent dipole-moment. These are known as polar crystals or ferroelectrics. Group theory demonstrates that the polar classes are: $m, mm2, 3m, 4mm$, and $6mm$. $LiTaO_3$ is a 3m class crystal and is therefore a ferroelectric material.

The poling process occurs when a strong electric field, called the coercive field, is applied to the material and the permanent dipole is reversed. The coercive field must be strong enough to overcome the potential barrier created by the crystal structure. This results in a permanent reversal of the crystal orientation in the region of the electric field. In the case of $LiTaO_3$ the coercive field must be $\sim$21 kV/mm for the reversal to occur [17].

The poling process can be implemented in a way that creates micro-patterned domain reversal. This was the process used to create the the domain pattern shown in Figure 1.2 in the device under study. The process has limitations such as the thickness of the poled material. The devices tested were fabricated at PSU on $\sim$0.286 mm thick lithium tantalate. The two devices tested were found to have some defects in operation that were believed to originate in the packaging process. Efforts were made toward fabricating additional devices. These efforts are detailed in Chapter III. The wafers poled in-house were 0.5 mm thick.

2.4 Anisotropic Medium

This section will develop the relationships between the polarization of propagating light and the refractive index of some types of media. It then progresses to the electro-optic effect and the application to the operation of this device. These sections are adapted mainly from [2], [12] and [21].

2.4.1 Nonlinear Theory. The optical properties of isotropic materials do not depend upon the direction of propagation nor on the polarization of the light. The induced polarization is parallel and linearly related to the electric field and can be described by the following relationship

$$\mathbf{P} = \varepsilon_0 \chi \mathbf{E} \tag{2.10}$$

where the two scalars are ε_0, the permittivity of a vacuum, and χ, the linear susceptibility of the medium.

However, the device under study is fabricated from $LiTaO_3$ which is not isotropic. In $LiTaO_3$ and all other anisotropic materials the scalar χ becomes a rank 2 tensor and the induced polarization depends upon the polarization of the light. Using tensor notation the polarization relationship is

$$P_i = \varepsilon_0 \chi_{ij} E_j \tag{2.11}$$

or explicitly,

$$\begin{bmatrix} P_1 \\ P_2 \\ P_3 \end{bmatrix} = \varepsilon_0 \begin{bmatrix} \chi_{11} & \chi_{12} & \chi_{13} \\ \chi_{21} & \chi_{22} & \chi_{23} \\ \chi_{31} & \chi_{32} & \chi_{33} \end{bmatrix} \begin{bmatrix} E_1 \\ E_2 \\ E_3 \end{bmatrix}. \tag{2.12}$$

Recalling the following material equation describing the relationship between the electric displacement, $\mathbf{D}$, and the electric field, $\mathbf{E}$, is

$$D_i = \varepsilon_0 E_j + P_j = \varepsilon_{ij} E_j \tag{2.13}$$

where ε_{ij}, called the dielectric or permittivity tensor, represents nine constants or material parameters that are dependant upon the material and its orientation. Equation 2.13 implies

$$\varepsilon_{ij} = \varepsilon_0 \left(1 + \chi_{ij}\right) \tag{2.14}$$

and so the explicit relationship between $\mathbf{D}$ and $\mathbf{E}$ is thus

$$\begin{bmatrix} D_1 \\ D_2 \\ D_3 \end{bmatrix} = \begin{bmatrix} \varepsilon_{11} & \varepsilon_{12} & \varepsilon_{13} \\ \varepsilon_{21} & \varepsilon_{22} & \varepsilon_{23} \\ \varepsilon_{31} & \varepsilon_{32} & \varepsilon_{33} \end{bmatrix} \begin{bmatrix} E_1 \\ E_2 \\ E_3 \end{bmatrix}. \tag{2.15}$$

For a lossless material the permittivity tensor, ε, is real. If it is also a non-optically active material, the permittivity tensor is symmetric. Therefore, the coordinate system for the dielectric tensor can be rotated in such a way that the off-axis elements vanish. This creates a new principle-axis system where the dielectric tensor is a diagonal matrix. The relationship in Equation 2.15 can now be express in the simpler form

$$\begin{bmatrix} D_x \\ D_y \\ D_z \end{bmatrix} = \begin{bmatrix} \varepsilon_x & 0 & 0 \\ 0 & \varepsilon_y & 0 \\ 0 & 0 & \varepsilon_z \end{bmatrix} \begin{bmatrix} E_x \\ E_y \\ E_z \end{bmatrix}, \tag{2.16}$$

where ε_x, ε_y and ε_z are the principal dielectric constants. Equation 2.16 can be equivalently expressed as

$$\begin{bmatrix} E_x \\ E_y \\ E_z \end{bmatrix} = \begin{bmatrix} \frac{1}{\varepsilon_x} & 0 & 0 \\ 0 & \frac{1}{\varepsilon_y} & 0 \\ 0 & 0 & \frac{1}{\varepsilon_z} \end{bmatrix} \begin{bmatrix} D_x \\ D_y \\ D_z \end{bmatrix}. \tag{2.17}$$

The energy per unit volume of the electric field component of a wave propagating through an anisotropic medium that is also homogeneous, nonabsorbing and magnetically isotropic is

$$U = \frac{1}{2}\mathbf{E} \cdot \mathbf{D}. \tag{2.18}$$

By substituting Equation 2.17 in Equation 2.18, the energy density can be expressed thus,

$$2U = \begin{bmatrix} \frac{1}{\varepsilon_x} & 0 & 0 \\ 0 & \frac{1}{\varepsilon_y} & 0 \\ 0 & 0 & \frac{1}{\varepsilon_z} \end{bmatrix} \begin{bmatrix} D_x \\ D_y \\ D_z \end{bmatrix} \cdot \begin{bmatrix} D_x \\ D_y \\ D_z \end{bmatrix} \tag{2.19}$$

or

$$2U = \frac{D_x^2}{\varepsilon_x} + \frac{D_y^2}{\varepsilon_y} + \frac{D_z^2}{\varepsilon_z}. \tag{2.20}$$

Finally by setting

$$\mathbf{r} = \frac{\mathbf{D}}{\sqrt{2U}} \tag{2.21}$$

we can express the surface of constant energy density in real space as the index ellipsoid thus,

$$\frac{x^2}{n_x^2} + \frac{y^2}{n_y^2} + \frac{z^2}{n_z^2} = 1. \tag{2.22}$$

This index ellipsoid equation is used to find the index of refraction for the two components of light propagating through an anisotropic medium. In the case of a uniaxial crystal, where $n_x = n_y \neq n_z$, n_x and n_y can be represented as the ordinary index, n_o and n_z as the extraordinary index, n_e. Lithium tantalate is a positive uniaxial crystal, which means n_e is larger than n_o.

2.4.2 The Electro-Optic Effect. The electro-optic effect is the change in refractive index of a material induced by the presence of a dc electric field. Some materials experience a linear dependance of the index on the electric field. This is called the linear electro-optic effect or Pockels effect.

The impermeability tensor, η_{ij}, for a crystal with no applied electric field can be expressed in terms of the refractive indices as follows

$$\eta = \begin{bmatrix} \frac{1}{n_x^2} & 0 & 0 \\ 0 & \frac{1}{n_y^2} & 0 \\ 0 & 0 & \frac{1}{n_z^2} \end{bmatrix}. \tag{2.23}$$

Also, the change in the impermeability tensor induced by an electric field can be written

$$\eta_{ij}(\mathbf{E}) - \eta(0) = r_{ijk}E_k \tag{2.24}$$

where $\mathbf{E}$ is the applied electric field and $\eta_{ij}(\mathbf{E})$ is the impermeability tensor with the applied electric field, $\eta(0)$ is the impermeability tensor with no electric field applied and r_{ijk} is the tensor that describes the linear electro-optic effect. As the notation suggests, the electro-optic coefficient tensor, r_{ijk}, is a third-rank tensor. However, because η_{ij} is real and symmetric, r_{ijk} is also symmetric in its first two indices (i.e., $r_{ijk} = r_{jik}$) and the following contracted notation can be used

$$\begin{aligned} r_{1k} &= r_{11k} \\ r_{2k} &= r_{22k} \\ r_{3k} &= r_{33k} \\ r_{4k} &= r_{23k} = r_{32k} \\ r_{5k} &= r_{13k} = r_{31k} \\ r_{6k} &= r_{12k} = r_{21k}. \end{aligned} \tag{2.25}$$

According to the contracted notation from Equation 2.25 the electro-optic coefficient tensor is written in the form

$$\begin{pmatrix} r_{11} & r_{12} & r_{13} \\ r_{21} & r_{22} & r_{23} \\ r_{31} & r_{32} & r_{33} \\ r_{41} & r_{42} & r_{43} \\ r_{51} & r_{52} & r_{53} \\ r_{61} & r_{62} & r_{63} \end{pmatrix}. \tag{2.26}$$

Equation 2.23 can now be expressed as

$$\eta = \begin{bmatrix} \frac{1}{n_x^2} + r_{1k}E_k & r_{6k}E_k & r_{5k}E_k \\ r_{6k}E_k & \frac{1}{n_y^2} + r_{2k}E_k & r_{4k}E_k \\ r_{5k}E_k & r_{4k}E_k & \frac{1}{n_z^2} + r_{3k}E_k \end{bmatrix}. \tag{2.27}$$

When Equation 2.27 is combined with Equation 2.18 and a similar development made the index ellipsoid is expressed as follows,

$$x^2\left(\frac{1}{n_x^2} + r_{1k}E_k\right) + y^2\left(\frac{1}{n_y^2} + r_{2k}E_k\right) + z^2\left(\frac{1}{n_z^2} + r_{3k}E_k\right) + 2yzr_{4k}E_k + 2xzr_{5k}E_k + 2xzr_{6k}E_k = 1. \tag{2.28}$$

Equation 2.26 is the general form of the electro-optic coefficient tensor. The specific form the tensor takes on is determined by the crystal symmetry and is therefore dependant on the material used. For $LiTaO_3$, which is a trigonal crystal belonging to the 3m symmetry group, the electro-optic coefficient tensor is described in Table 2.1.

Our device operates with an electric field applied across the c-axis (i.e., in the z direction, so k=3 in Equation 2.28) of the $LiTaO_3$ crystal. Notice the r_{43}, r_{53} and r_{63} terms are zero for both forms of the tensor in Table 2.1. This eliminates the last three terms from Equation 2.28. Also, recalling that $LiTaO_3$ is a uniaxial crystal, n_x and n_y can be replaced with n_o and n_z can be replaced with n_e. This allows the

Table 2.1: Electro-optic coefficients for trigonal 3m crystals.

3m (m $\perp x_1$)	3m (m $\perp x_2$)
$\begin{pmatrix} 0 & -r_{22} & r_{13} \\ 0 & r_{22} & r_{13} \\ 0 & 0 & r_{33} \\ 0 & r_{51} & 0 \\ r_{51} & 0 & 0 \\ -r_{22} & 0 & 0 \end{pmatrix}$	$\begin{pmatrix} r_{11} & 0 & r_{13} \\ -r_{11} & 0 & r_{13} \\ 0 & 0 & r_{33} \\ 0 & r_{51} & 0 \\ r_{51} & 0 & 0 \\ 0 & -r_{11} & 0 \end{pmatrix}$

electro-optically changed index ellipsoid to be written

$$x^2\left(\frac{1}{n_o^2}+r_{13}E\right)+y^2\left(\frac{1}{n_o^2}+r_{13}E\right)+z^2\left(\frac{1}{n_e^2}+r_{33}E\right)=1. \tag{2.29}$$

To find the change in the index caused by the applied electric field we make use of the fact that

$$\frac{d}{dn}(n^{-2})=-2n^{-3} \tag{2.30}$$

for small Δn. Also, from Equation 2.29 it is evident that $\Delta\left(\frac{1}{n_o^2}\right)=r_{13}E$ and $\Delta\left(\frac{1}{n_e^2}\right)=r_{33}E$. Therefore, substituting in Equation 2.30 allows

$$\begin{aligned} r_{13}E &= -2\tfrac{1}{n_o^3}\Delta n_o \\ r_{33}E &= -2\tfrac{1}{n_e^3}\Delta n_e \end{aligned} \tag{2.31}$$

or equivalently,

$$\begin{aligned} \Delta n_o &= -\tfrac{1}{2}n_o^3 r_{13}E \\ \Delta n_e &= -\tfrac{1}{2}n_e^3 r_{33}E. \end{aligned} \tag{2.32}$$

The new indices are expressed as

$$\begin{aligned} n_x &= n_o' = n_o - \tfrac{1}{2} n_o^3 r_{13} E \\ n_y &= n_o' = n_o - \tfrac{1}{2} n_o^3 r_{13} E \\ n_z &= n_e' = n_e - \tfrac{1}{2} n_e^3 r_{33} E. \end{aligned} \tag{2.33}$$

where n_o' is the electro-optically changed n_o and n_e' is the electro-optically changed n_e. Therefore, in this case, the crystal remains uniaxial.

2.4.3 Device Operation. Our device is designed for light polarized parallel to the z-axis. Light that is polarized along the z-axis will only experience n_e' and only the change in that index is important. Recall from Equation 2.8 that one of the important parameters for beam deflection is the the change in index across an interface, Δn.

To find Δn across the interface of a periodically poled lithium tantalate crystal, first notice in Equation 2.33 that an electric field parallel to the c-axis will cause a drop in the index while an antiparallel electric field will cause a rise in the index due to the sign of the electric field. So, a uniform electric field applied across a periodically poled crystal will induce a periodically modulated index as in Figure 2.7.

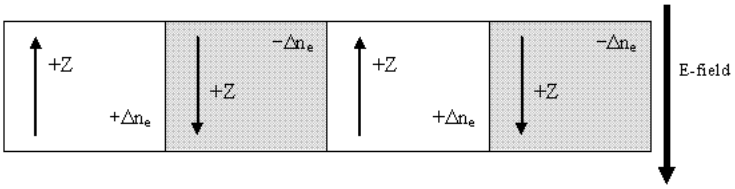

Figure 2.7: The electric field induced index change in a periodically poled lithium tantalate crystal.

In the parallel regions the index is $n_e - \frac{1}{2} n_e^3 r_{33}|E|$ and in the antiparallel regions the index is $n_e + \frac{1}{2} n_e^3 r_{33}|E|$. Therefore,

$$\Delta n = n_e'^{(antiparallel)} - n_e'^{(parallel)} = (n_e + \frac{1}{2} n_e^3 r_{33}|E|) - (n_e - \frac{1}{2} n_e^3 r_{33}|E|) = n_e^3 r_{33}|E|. \tag{2.34}$$

where $n_e'^{(antiparallel)}$ and $n_e'^{(parallel)}$ are the electro-optically changed indices of the antiparallel and parallel regions respectively.

Now that the expression for Δn has been found it can be plugged into Equation 2.8. The new equation is written

$$\theta_{int} = n_e^2 r_{33} |E| \frac{L}{W}. \tag{2.35}$$

The width of each channel, W, was designed to be approximately .5 mm to match an available lens array. Each stage has a length, L, of about 1 cm. Therefore, with $n_e = 2.1403$ and $r_{33} = 29.14 \times 10^{-12}$ m/V [8, 16] at the operating wavelength, λ, of 1.064 μm, the electric field can be calculated as follows. First, given a desired external deflection per stage of about 2°, the internal deflection angle, θ_{int}, is found from Equation 2.9 to be .94°. Equation 2.35 is used to calculate the electric field as as below

$$E = \frac{W\theta_{int}}{n_e^2 r_{33} L} \approx 5kV/mm. \tag{2.36}$$

A device thickness of .286 mm therefore, requires an applied voltage of 1.4 kV for maximum deflection of 2°.

III. Device Fabrication

3.1 Introduction

All of the data presented in Chapter V are from experiments conducted with two devices fabricated at Penn State Materials Research Institute. However, work on fabricating additional devices was conducted locally using techniques similar to the Penn State procedures but adapted for local equipment using the expertise and advise from Eric Vershure in AFRL/SNJW. Much of the information in this section is adapted from the Vershure Master Thesis [20]. The mask used in processing the devices has the pattern for two devices. Two wafers were patterned in this fabrication work for a total of four devices.

3.2 Material

The Penn State University (PSU) devices were fabricated on z-cut single crystal $LiTaO_3$ wafers which were $\sim$286.5 μm thick. The locally fabricated devices were also on z-cut single crystal $LiTaO_3$ wafers but the thickness was 500 μm. These wafers were received with two flats of different lengths cut on the edge of the wafer to indicate orientation. Conventionally, these flats obey the right hand rule such that the long flat crossed with the short flat indicates the +z direction in lithium tantalate. This is opposite of the convention used for other materials such as lithium niobate. However, no instructions were received to indicate which convention was followed and communication with the manufacturer did not clear up the question. Previous confusion on wafer orientation from this manufacturer forced us to fabricate two sets of devices. One wafer was processed assuming the long-cross-short convention and the other assuming the short-cross-long convention. Later it was discovered that the wafers follow the long-cross-short convention as discussed in the following sections.

3.3 Patterning

The patterning steps described here were performed in a class 100 clean room environment. Shipley SC 1827 positive photo-resist was applied to the wafers center

covering about two-thirds of the surface. The resist was spun on at 400 rpm for 2 seconds, followed immediately by a 4000 rpm, 30 second spin cycle. The wafers were then transferred to a 60° C soft-bake oven, where the solvents were evaporated for 30 minutes.

The mask pictured in Figure 3.1 was used to define the device pattern on the z face of the crystal surface. The mask was designed by Penn State researchers using Matlab code based on the beam deflection design principles laid out in Chapter II and elsewhere [5, 17]. The specifications of the channels and stages of the mask are given in Table 3.1

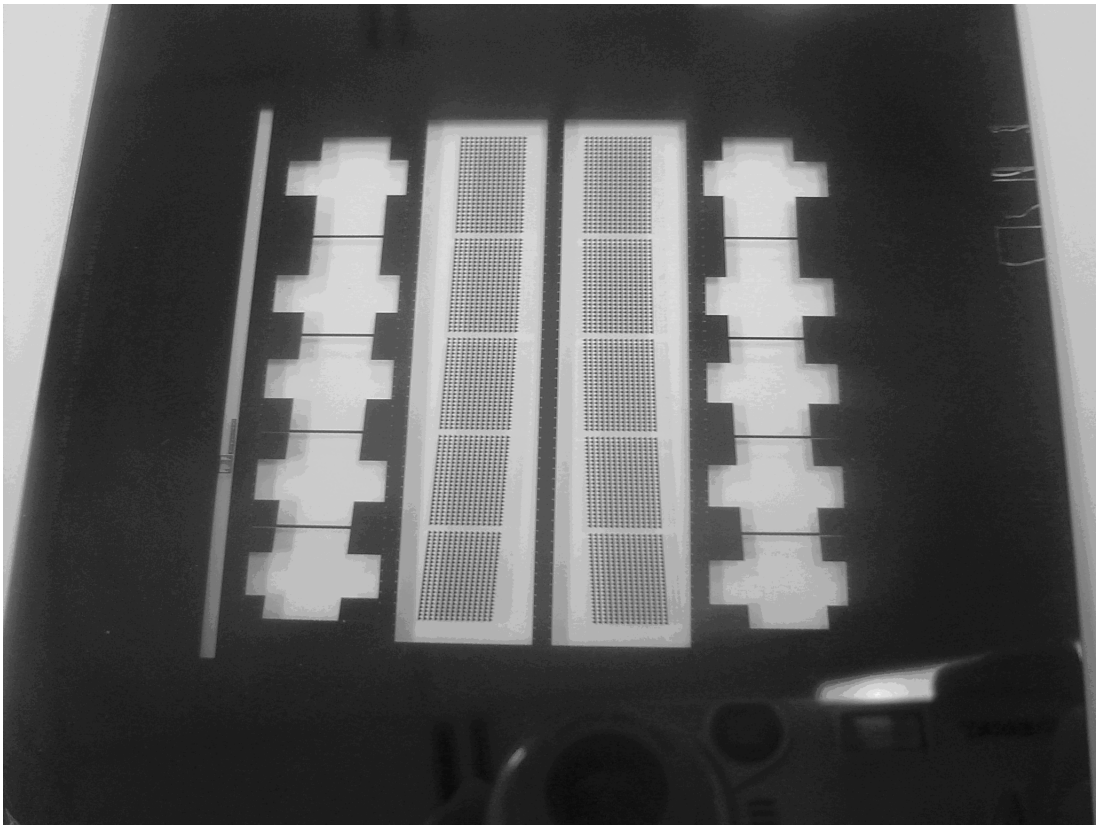

Figure 3.1: Photo-mask used for device fabrication.

A photo-mask shield made from aluminum foil was used to isolate the main device structures from the contact pad patterns meant for patterning later in the fabrication process as in Figure 3.2. The foil prevented exposing contact patterns onto the wafer at this time. The mask and wafer were exposed for 45 seconds in

Table 3.1: Scanner Specifications.

	Stage 1	Stage 2	Stage 3	Stage 4	Stage 5	Total
Width, W (mm)	0.444	0.410	0.383	0.362	0.348	8.31
Length, L (mm)	11.16	10.209	9.45	8.852	8.41	50
Field (kV/mm)	5	5	5	5	5	5
Int. angle, θ_{int} (degrees)	.96	.95	.94	.93	.92	4.72
Ext. angle, θ_{ext} (degrees)	2.06	2.04	2.02	2.00	1.98	10.13

a Karl Suss MJB-3 mask aligner, followed by development of the resist in Shipley Microposit 351 Developer for 1 minute with gentle agitation. Next, the wafers were rinsed in deionized water for one minute and hard-baked at 105° C for two hours with a 40-minute ramp-up/ramp-down time. Finally, 200 angstroms of chrome and 2000 angstroms of gold were evaporated onto the pattern. The devices from PSU were fabricated with tantalum electrodes instead of the gold and chrome but this should have no effect on device operation. A cross section representation of the wafer at this point is shown in Figure 3.3. The resist pattern remaining acts to reduce surface conduction and suppresses domain reversal in the regions where the metal is not in direct contact with the crystal.

3.4 Poling

An apparatus consisting of two Plexiglass plates with hollow tubes and o-ring recessions milled out of them was used to hold the wafer during poling as seen in Figure 3.4 below. The plates sandwiched the wafer between the two insulating o-rings with four set-screws. A liquid-electrolyte solution consisting of 3:2 ratio-by-weight of distilled water to reagent-quality granular LiCl was injected into the disk-shaped spaces between the plate and the wafer on each side with a syringe. High-voltage leads were placed in contact with the solution on each side, and connected to the poling circuit.

The poling circuit in Figure 3.5 is a voltage divider, driven by a Trek 620N high-voltage amplifier. The voltage divider circuit allows the voltage level to be

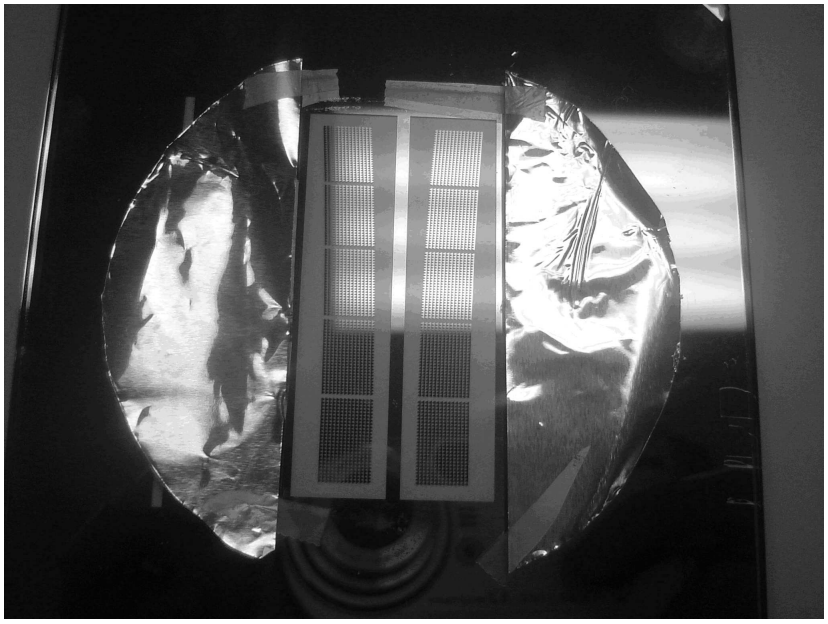

Figure 3.2: Photo-mask with aluminum foil shield.

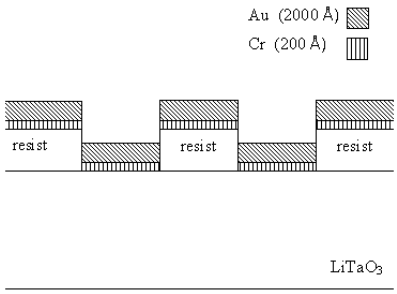

Figure 3.3: Cross-section of wafer after metalization.

monitored and controlled via a computer program. The values of the resistors were: $R_L = 100M\Omega$, R1 and R2 = $1G\Omega$, and $R_M = 100k\Omega$. R_L serves as a current-limiting resistor which forces a slow poling process. The monitoring resistor, R_M, is used to provide feedback to the controlling program. The voltage drop across R_M is monitored via a *National Instruments* analog-to-digital data acquisition (DAQ) card. The value of R_M was matched to the current limiter such that when the current was at its limit, the voltage across R_M would be roughly 5 V which is less than the saturation level of the DAQ card.

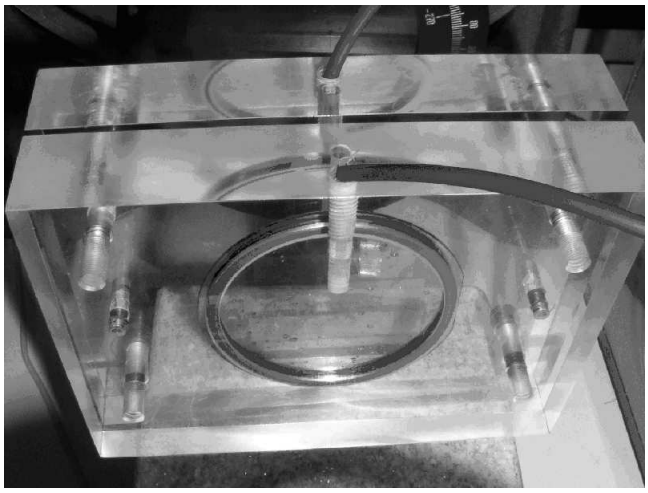

Figure 3.4: Poling mount. A non-metallized wafer is sandwiched between two o-rings.

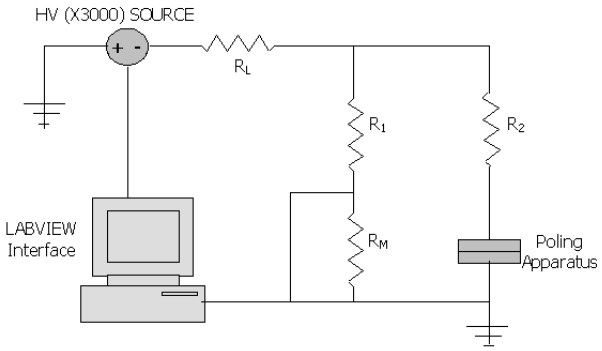

Figure 3.5: Poling circuit. The poling apparatus is placed in parallel with a voltage divider.

A user interface, written in Labview provided the logic necessary to monitor and control the poling process. The interface allows control of the number of ramp-up/down steps, the total charge to be delivered, and the target voltage to be applied. The interface logic uses the voltage drop across R_M to create plots of the voltage across the crystal. The operator determines the amount of total charge to be deposited by multiplying the area to be poled by the material charge density (80 μC/cm^2 for CLT). The program first ramps up to the voltage level specified by the operator, which is based on the coercive field for the material and the thickness of the wafer. It maintains this level long enough to deposit the total amount charge entered by the operator. The program then ramps down the voltage. The measured voltage does not follow

the perfect traces as just described because it reflects the varying voltage drop that occurs as the poling process progresses. Two example poling voltage traces [20] from previous samples of lithium niobate are seen in Figure 3.6 (a) and (b), and an example of poling of a stoichiometric lithium tantalate crystal (2.0-mm thick) sample in (c). Notice the slightly different poling patterns between the different materials. This reflects the differences in the poling process of the materials. The material used for the current fabrication efforts were congruent lithium tantalate (CLT).

The electric field required to cause domain inversion, or coercive field for CLT is 21 kV/mm [17]. It has been reported [20] that poling is successful when the applied field is around 115% of the coercive field. The field applied for poling in here was 22.4 kV/mm which is 107%. Notice that the field used for SLT in Figure 3.6(c) only reaches a maximum value of about 3 kV across 2 mm. This is because the coercive field for SLT is 1.7 kV/mm. The poling voltage traces are shown for the two wafers poled for scanning device fabrication in Figures 3.7.

The poling pattern in the long-cross-short wafer shown in Figure 3.7(a) is similar, although not identical, to that of SLT. Both have a gradual increase in poling voltage early in the process followed by an upturn. The CLT sample used (Figure 3.7(a)) has a gradual decrease in the voltage, while SLT (Figure 3.6(c)) continues with a gradual increase. Another difference is the time of poling. The poling time is based on the operator controlled parameter of the amount of charge deposited during the poling process. It was discovered during inspection, covered in the next section, that over-poling occurred on this wafer. It is likely that the longer poling time shown in Figure 3.7(a) was too long meaning the integrated charge was too high. The other CLT wafer (short-cross-long) in Figure 3.7(b) had a pattern totally uncharacteristic of lithium tantalate. This was the first indication that the manufacturer followed the long-cross-short convention for these wafers, because it didn't pole as expected.

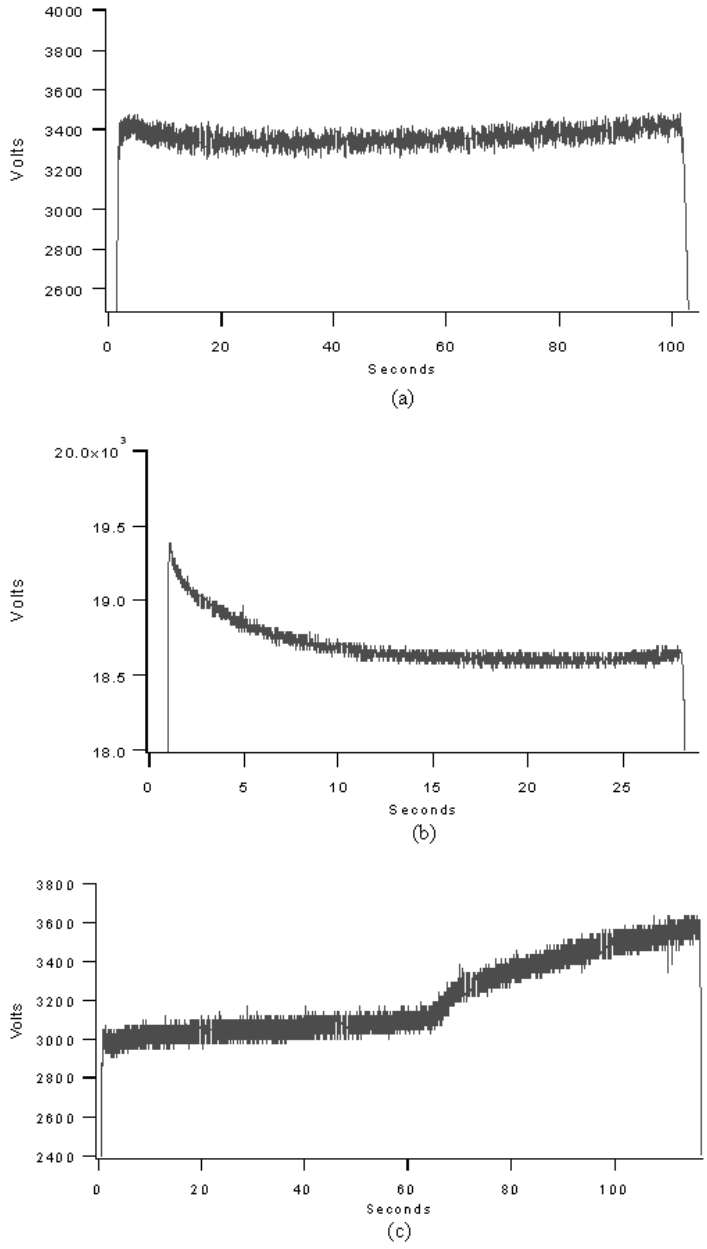

Figure 3.6: Poling voltage charts. (a) typical poling voltage for 1.0mm thick stoichiometric lithium niobate (SLN), (b) typical poling voltage for 1.0mm thick congruent lithium niobate (CLN), (c) typical poling voltage for 2.0mm thick stoichiometric lithium tantalate (SLT).

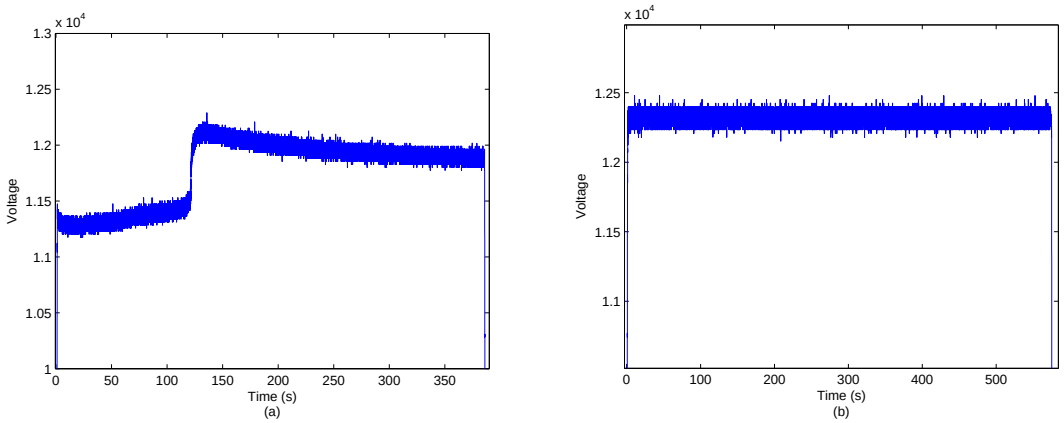

Figure 3.7: Poling voltage charts. (a) assumed to have the long-cross-short orientation, (b) assumed to have the short-cross-long orientation.

3.5 Inspection

The +z face etches at a different rate than does the -z face. To aid in inspecting the poling results the wafers were etched in 49% hydrofluoric acid (HF) until patterns were visible. Based on previous experience with SLT, the CLT was etched for 30 minutes. After etching, the patterns were viewed under an illumination microscope. Several types of poling defects are well known, including under-poling (missing domains), domain broadening, incomplete-poling (partial domains), or over-poling. Figure 3.8 shows a periodically poled lithium niobate sample with mostly clean poling except for a few missing domains. This is presented here as a point of comparison for the poling images for the $LiTaO_3$ wafers.

It was found that no poling was visible in the lithium tantalate sample assumed to be of the short-cross-long convention. This was the same wafer that had had the uncharacteristic poling voltage trace. It was therefore concluded that the wrong orientation had been assumed for this wafer.

The long-cross-short sample did show poling. In fact, there were indications of over-poling. In Figure 3.9, there are large smooth triangles with well defined boundaries that indicate successful poling. However, the surface in the adjacent regions should also be smooth which would indicate an un-poled area. Instead there are

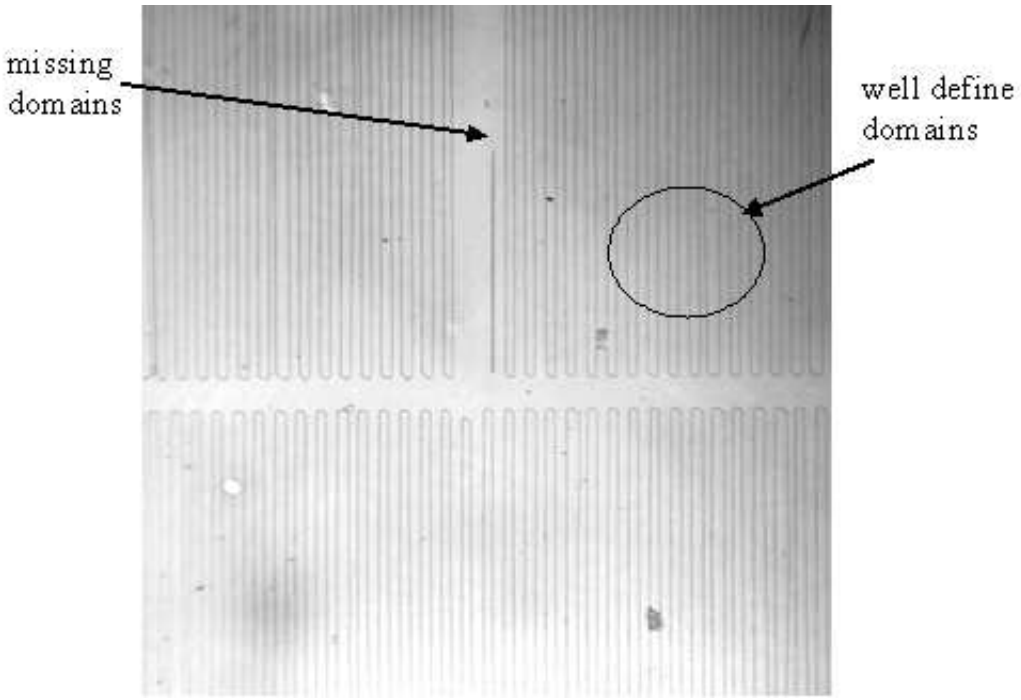

Figure 3.8: -z surface of periodically poled SLN with incomplete/missing domains and well defined domains

small irregular triangles within the un-poled regions indicating the formation of reversed domains. There are some regions of the wafer where the over-poled domains were very populous. Figures 3.10 and 3.11 show various levels of over-poling across the wafer.

Due to the unsuccessful poling step and time constraints, no additional fabrication steps were completed. However, the partial success that was achieved provided some insight into the possibility of achieving full success in future attempts in follow-up work. The poling process should be shorter than the 400 sec as seen in Figure 3.7 to prevent over poling. One possibility is to stop poling at the point of the sharp increase in poling voltage. This increase could come from current leakage that defeats the resist which normally protects the regions which are not intended to be poled. Several attempts may be necessary to find the appropriate poling time for this material.

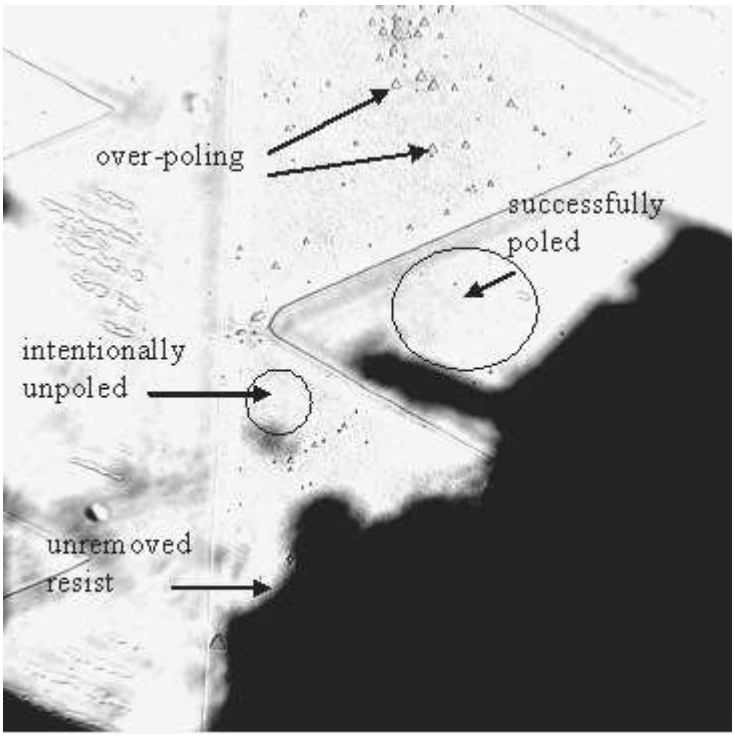

Figure 3.9: Picture of device where there is light over-poling.

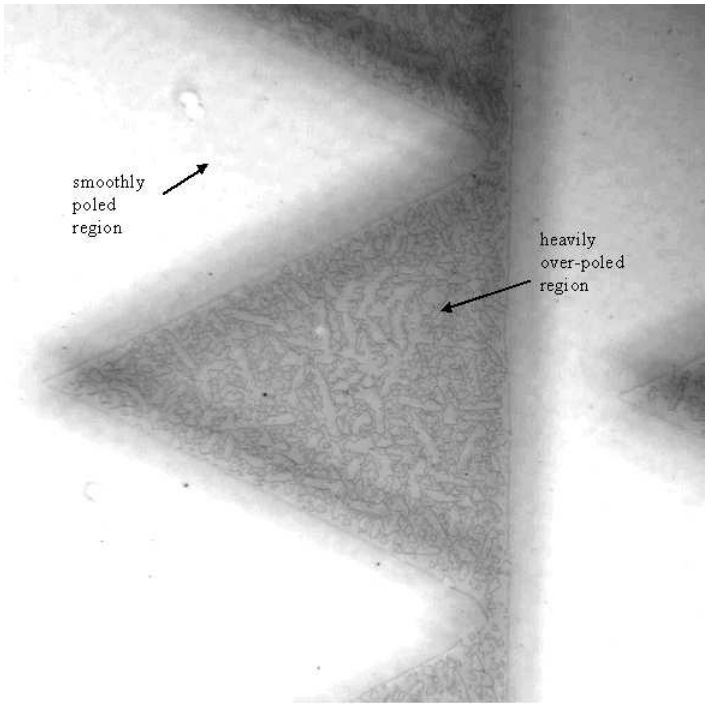

Figure 3.10: A heavily over-poled region.

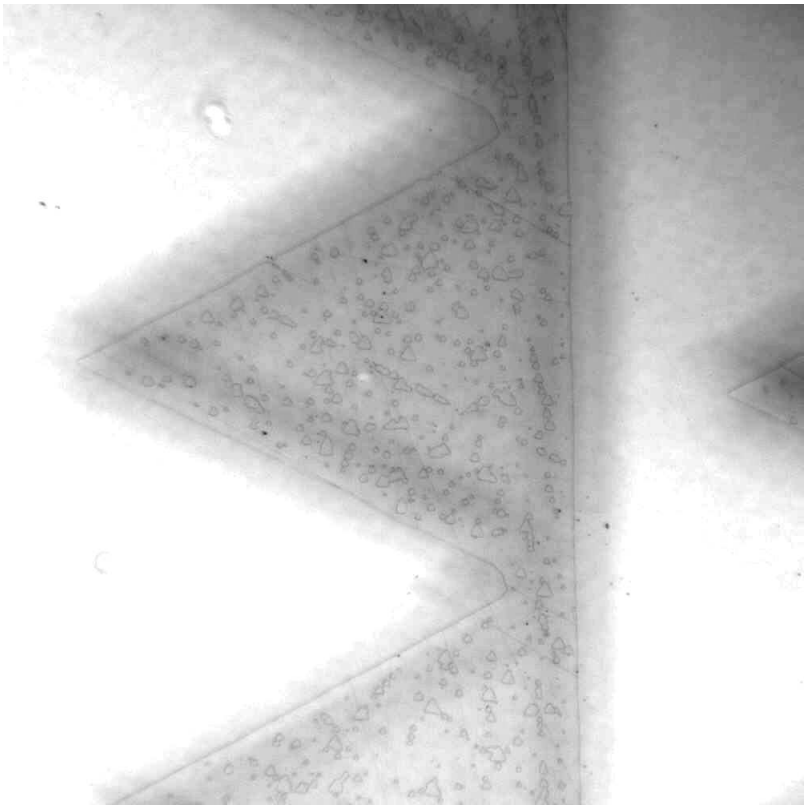

Figure 3.11: More over-poling.

3.6 Final Device Preparations and Packaging

Because of the over-poling, the devices were not prepared for final packaging. However, additional patterning and metallization for the individual stage contacts and the common ground would normally be completed next. Then cutting and polishing of the devices would come next. The wafers would be cut into chips with a programmable dicing saw and then the input and the output faces polished. To polish the devices, sections of material of the same type and length are stacked together above and below the devices. The stack is then mounted on a block and set in a polishing jig. First the device is polished by hand lapping and then in an auto-polisher. Polishing is finished when no scratches are visible at 30x magnification. This was previously determined to generally take between a half-hour and several hours [20], depending on how flush the stack was prior to hand-lapping. Longer hand-lapping creates deeper scratches which take longer to polish away.

After polishing, devices must be packed for operation. Although one of the two PSU devices tested here was annealed to remove any lattice damage that may have been caused by the domain reversal process, there was only minor difference in performance between the annealed and the un-annealed devices. Contact with the electrodes was established with copper tape, and the device was then mounted between two insulating rubber layers to further inhibit discharge during operation. It also helped to have the device fastened to a microscope slide to provide for stable placement in the device mount. One of the tested devices was not packaged onto a slide. The bottom of this device packaging was the bottom rubber layer which was uneven and made beam alignment inconsistent. However, the other device which was packaged onto the slide had more consistent alignment.

IV. Experimental Setup and Methodology

4.1 Introduction

This chapter presents the experimental setup and procedures used. The chapter is separated into equipment and procedures common to all experiments, those used for the single-stage experiments, and finally the setup for the multi-stage experiments.

4.2 General Equipment and Procedures

4.2.1 Experimental Devices. Two devices were tested in the course of this research. Although efforts were made to fabricate additional devices locally, this work was unsuccessful and did not result in a working device. See the previous chapter on fabrication for a description of the fabrication efforts.

The two working devices tested were provided by the Materials Research Institute of Penn State University. There are some unintended differences between the two devices tested. The annealing step was omitted during the fabrication of one of the devices. Annealing as described in Chapter III was accomplished in an attempt to repair any damage to the crystal structure that may have been caused during the poling process. Additionally, the exit face of this device was inadvertently polished at an angle of 1.82° from parallel to the entrance face. This device is called device 1 through the remainder of this thesis. The other device, device 2, had stage four and five electrically shorted together. Therefore, these two stages could not be controlled independently. Figure 4.1 shows images of the two devices.

Each device had a total of six copper ribbons, one for each of the five stages and one for the common ground as seen in the cross-section diagram of the device in Figure 4.2. The two devices were designed to steer in opposite directions. Both devices in Figure 4.1 have the entrance face on the right and the beam propagates to the exit face on the left. Device 1 deflects the beam toward the right when looking in the direction of beam propagation. Device 2 deflects the beam to the left.

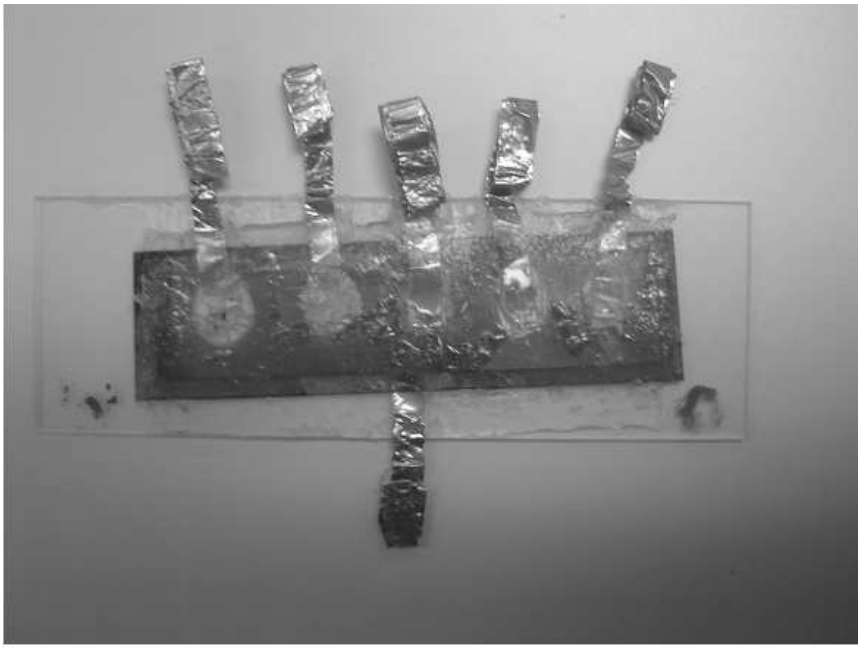

(a)

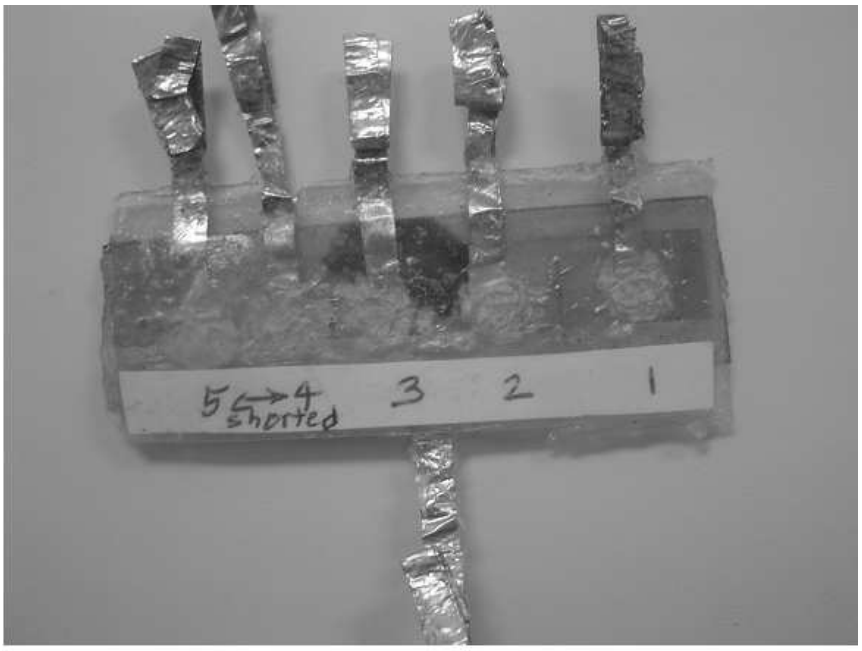

(b)

Figure 4.1: The two working devices (a) device 1, (b) device 2.

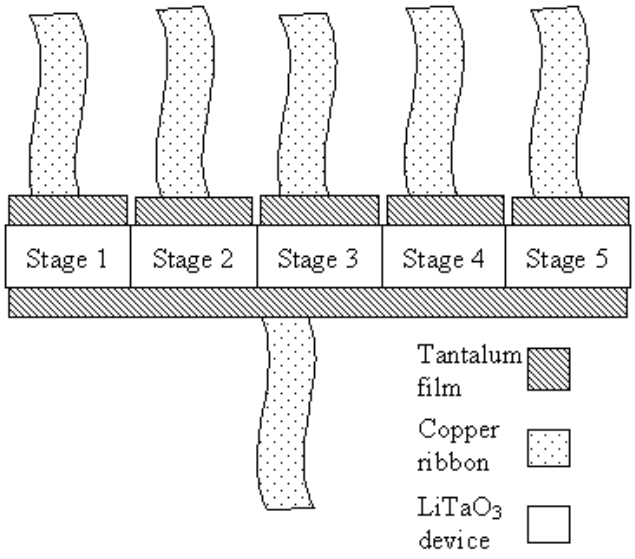

Figure 4.2: Diagram of the cross-section of the devices tested.

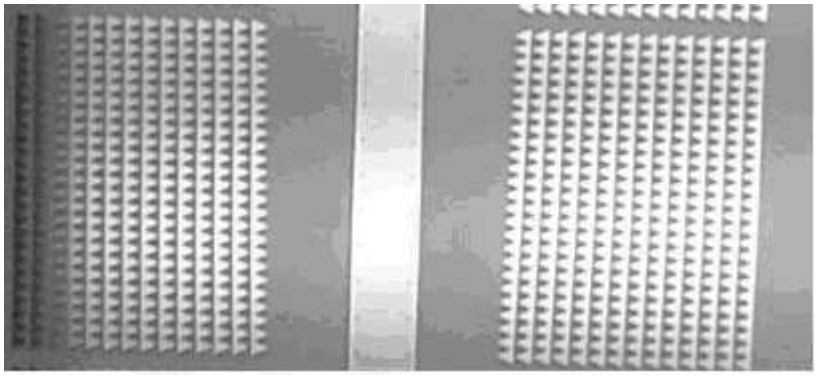

Figure 4.3: Closeup of the mask showing the oppositely facing orientations of the prisms for the two devices.

The mask, as shown in Figure 3.1, has the pattern for two devices on it each designed to deflect in opposite directions. The closeup in Figure 4.3 shows the prisms of the two devices oriented in opposite directions.

4.2.2 Experimental setup. The basic setup for all experiments is depicted in Figure 4.4. The laser is a Light Solutions, model LB10CV, Nd:YAG laser with the output wavelength, λ, equal to 1064 nm. The output of the laser was polarized vertically with respect to the optical bench which means an extraordinary polarization with respect to the device crystal. Recall from Chapter II that the device is designed

to steer only the extraordinary wave. Therefore a beam with both polarization components would be spilt, after passing through the device, the extraordinary beam being deflected as designed while the ordinary beam would experience no deflection. We confirmed this fact using a 633-nm unpolarized HeNe beam.

The beam expander is made up of two cylindrical lenses arranged such that they expand the beam horizontally to fill the entire extent of the lens array. The next cylindrical lens is used to focus the beam vertically to match the device thickness of 285 μm. The last optic before the scanner is the micro-lens array, which is a set of vertically oriented micro-lenses that are 500 μm across as seen in Figure 4.5. The lens array breaks up the beam into 14 beamlets spaced at the same distance as the channels of the scanning device.

There is also a high-voltage supply/amplifier used to drive the 14 device channel(s) to create the electro-optic effect for scanning. Two different high voltage supplies were used. One was only able to provide a single voltage level at a time. A second voltage supply was later built to enable five independent high voltage levels, one for each of the five stages.

4.2.3 Deflection Angle Measurement. Intensity profiles and beam positions were measured using a Coherent Cohu ER-5001 camera. Beam positions were recorded as a function of the driving voltage. To determine the precise beam location as the beam was scanned, it was necessary to block all but one of the beamlets by placing an adjustable slit between the lens array and the scanning device. This eliminated the confusion of recording the position of a different beam at any of the scanning levels.

Precise determination of the deflection angle from the beam position required at least two sets of measurements, each with the camera at a different distance from the scanning device. The location of the pivot point within the device varies depending on how many stages are being driven. Each stage has its own pivot point located at the center of that stage [5]. So, when only the first stage is active, the pivot point is located at the center of the first stage. As the other stages are activated the effective

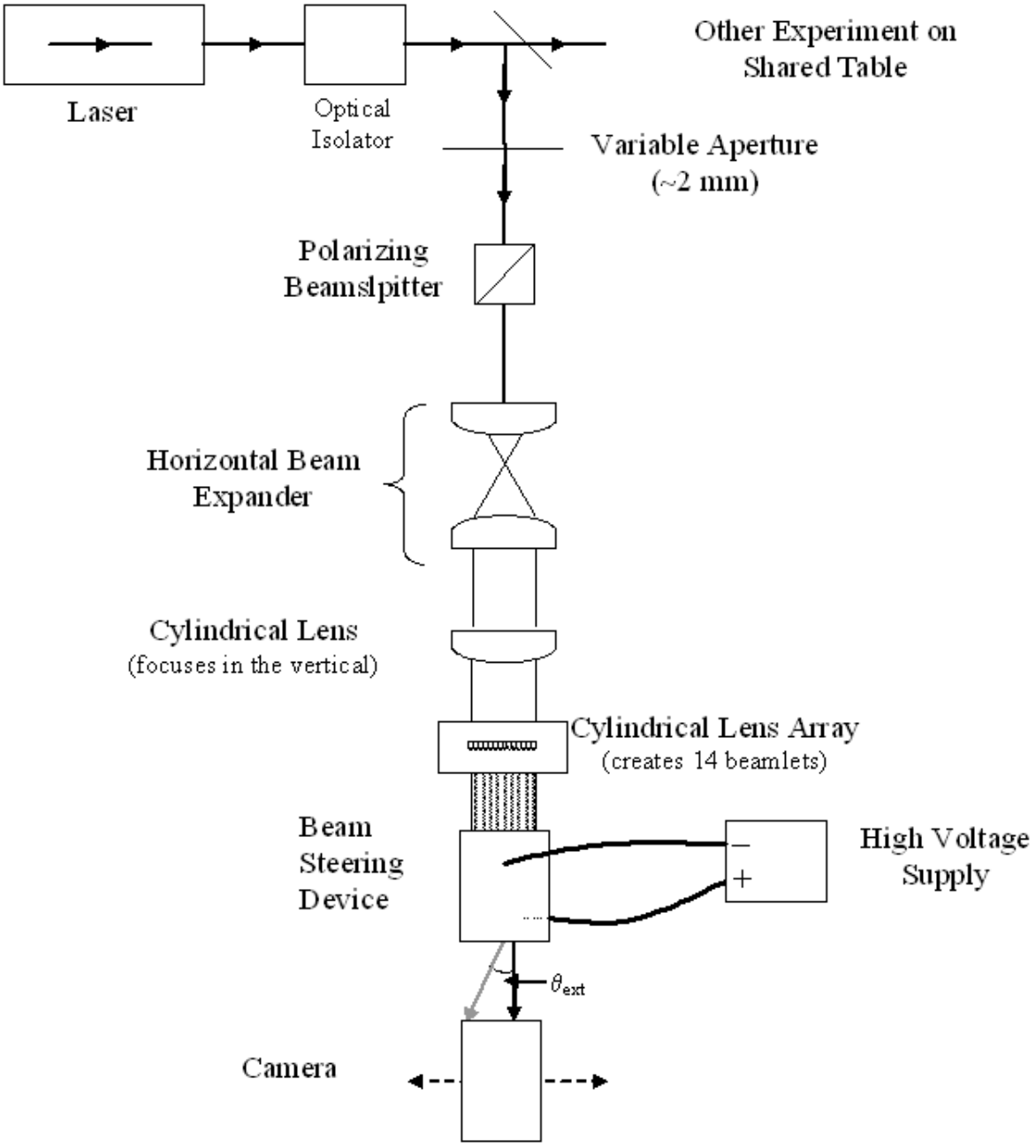

Figure 4.4: Basic setup used for all experiments

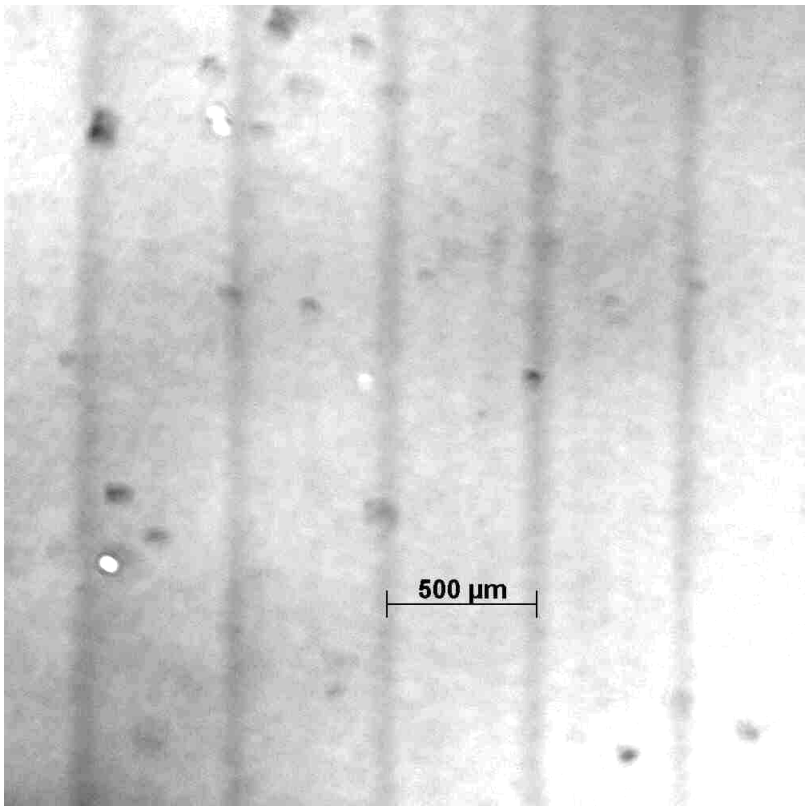

Figure 4.5: Picture of a portion of the micro-lens array taken with a microscope.

pivot point is shifted. Taking the measurements at two locations eliminated the need to know the location of the pivot point.

Figure 4.6 shows the setup and procedure for finding the deflection angle. The vertex of the large angle between the undeflected and deflected positions in the figure is the unknown variable pivot point of the device. The first step is to record a set of beam position measurements as a function applied voltage in the first plane. Then repeat the measurements in another plane that is a different distance from the device than the first plane. With the undeflected positions being set to zero, the measured relative positions at A2 and B2 can be subtracted as shown in the figure to find the opposite side of the smaller triangle that is congruent to the larger triangle.

The procedures above allow the deflection angle, θ, to be given by

$$\theta = tan^{-1}\left(\frac{opposite}{adjacent}\right) = tan^{-1}\left(\frac{B2 - A2}{Plane\ B - Plane\ A}\right). \tag{4.1}$$

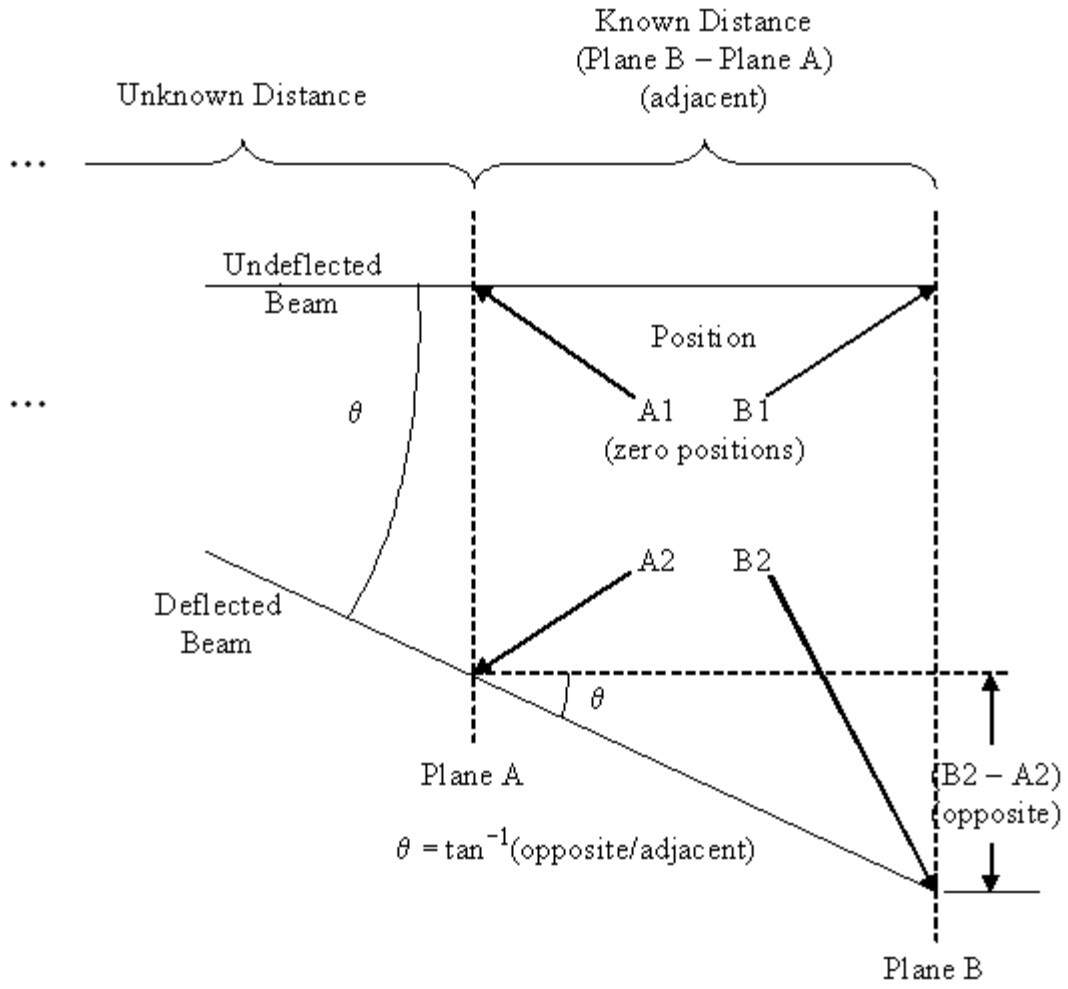

Figure 4.6: Procedure for deflection angle measurements.

The further apart the two planes are the less impact position measurement error will have on the results. This is because the measurement instruments will have the same uncertainty but the distances, B2-A2 (opposite side) and Plane B - Plane A (adjacent side), will be greater. As an example, Table 4.1 illustrates the the effect of error in distance measurements for two sample angle measurements.

4.2.4 Coupling Efficiency. A simple procedure was used to find the coupling efficiency of the device. A Laser Probe model Rk-570C power meter was inserted in the beam path in place of the camera in Figure 4.4. The total power of the beamlets was measured with the device in the path and properly aligned so that steering could

Table 4.1: Example of effect of distance measurement error on calculation of deflection angle.

(Plane B - Plane A) (cm) ($\pm 2.5mm$)	(B2 - B1) (mm) ($\pm 10\mu$m)	Angle (degrees)	Error (degrees)	Percent Error
12	19	9.0	± 0.2	± 2.10
29.5	47	9.1	± 0.1	± 0.85

be properly achieved. Then the device was removed and the the power level was again measured. This was repeated for both devices and at various deflection angles.

4.2.5 Far-field Measurements. The technique of imaging the far-field in the back focal plane of a lens is well known. The theory behind this techniques is widely understood but is briefly covered here for convenience. A complete coverage can be found in [9].

The Fresnel diffraction formula can be written

$$U(x\,y) = \frac{e^{ikz}}{i\lambda z} e^{i\frac{k}{2z}(x^2+y^2)} \int_{-\infty}^{\infty}\int_{-\infty}^{\infty} \{U(\xi,\eta) e^{i\frac{k}{2z}(\xi^2+\eta^2)}\} e^{-i\frac{2\pi}{\lambda z}(x\xi+y\eta)} d\xi d\eta, \tag{4.2}$$

where x and y are the dimensions in the diffraction plane, ξ and η are the dimensions in the source plane and z is the direction of propagation, k is the wave number and $U(\xi\,\eta)$ is the field in the source plane. Also, the phase transformation of a spherical lens is

$$t_l(x\,y) = exp\left[-i\frac{k}{2f}\left(x^2+y^2\right)\right]. \tag{4.3}$$

Thus, for a source field, $U_l(\xi,\eta)$, immediately in front of a spherical lens, the field immediately behind the lens is

$$U_l^{'}(\xi\,\eta) = U_l(\xi,\eta) exp\left[-i\frac{k}{2f}\left(\xi^2+\eta^2\right)\right]. \tag{4.4}$$

To find the field in the back focal plane of the lens, Fresnel diffraction in Equation 4.2 is used to propagate the field immediately behind the lens. Thus $z = f$ and Equation 4.4 is substituted into Equation 4.2,

$$U(x\,y) = \frac{e^{i\frac{k}{2f}(x^2+y^2)}}{i\lambda f} \int_{-\infty}^{\infty}\int_{-\infty}^{\infty} U_l(\xi,\eta) e^{-i\frac{k}{2f}\left(\xi^2+\eta^2\right)} e^{i\frac{k}{2f}(\xi^2+\eta^2)} e^{-i\frac{2\pi}{\lambda f}(x\xi+y\eta)} d\xi d\eta, \qquad (4.5)$$

where a constant phase was ignored. The first two phase factors in the integrand cancel each other and the equation can be simplified as

$$U(x\,y) = \frac{e^{i\frac{k}{2f}(x^2+y^2)}}{i\lambda f} \int_{-\infty}^{\infty}\int_{-\infty}^{\infty} U_l(\xi,\eta) e^{-i\frac{2\pi}{\lambda f}(x\xi+y\eta)} d\xi d\eta, \qquad (4.6)$$

This is the formula for the Fraunhofer (i.e., far-field) diffraction pattern. Therefore, the far-field image can be acquired in the lab by placing the camera at the back focal plane of a lens.

For this experiment the lens used was an anti-reflection coated lens with a focal length of 7.5 cm. The lens was placed at least 30 cm from the lens array. The lens array was found to introduce some complex phase fronts close to the output of the device (near field). However, regular beamlet patterns were observed at distances of around 30 cm.

4.3 Single Stage Experimental Setup

Early in the research effort only a single-stage high voltage supply and a single-stage mount shown in Figure 4.7, were available. A Trek model 610D high voltage amplifier/controller on loan from Penn State was used until a multi-stage supply was built. The Trek high-voltage device acted as both a supply and as an amplifier. The supply allowed the operator to manually set the dc voltage level or take a low-voltage modulated input signal and produce a high-voltage signal at 1000X the input. A function generator was used to provide input to the voltage amplifier.

Figure 4.7: Single-stage device mount with device 2.

The devices were operated in two modes under this configuration. The first mode had the power supply only connected to the first stage. In this mode the applied voltage could be varied from zero to the maximum voltage. The beam deflection at regular increments in that range were collected for stage one. The second mode had the single voltage supply connected to multiple stages. The stages were shorted together by connecting the copper ribbons to the single voltage lead and the voltage supply was set to maximum voltage. The maximum deflection of each set of stages was then recorded for the following groupings: stage 1 alone, stages 1 and 2, stages 1-3, stages 1-4, and stages 1-5. When the stages are shorted together the driving voltage must be at or near the maximum driving voltage so that each stage will deflect the beam to the appropriate angle for the beam to line up correctly for deflection in the subsequent stages.

4.4 Multiple Stage Experimental Setup

The single stage mount that was immediately available did not allow for the driving of each stage individually. A new mount was designed and fabricated that had the capability to deliver independently controlled voltage levels to the five separate stages. It also provided an easier method for switching between the two devices

being studied. The original mount required feeding the copper ribbons through a small vertical hole drilled under the BNC connectors as seen in Figure 4.7. Then the copper ribbon had to be soldered to the BNC connectors.

The new mount as seen in Figure 4.8 allowed for driving the individual stages independently. There are ten BNC connectors on the top of the mount seen in Figure 4.8(a). Only six of them are used at a time, five on one side to connect to the five individual stage leads and a sixth one to connect to the common ground. The mount also provided an easy method of switching the devices. The device is laid on the mounting plate seen in Figure 4.8(b) in the slot. The copper ribbons are then laid in the channels milled on the sides of the mounting plate as seen in Figure 4.8(c). The top mounting piece has spring loaded contacts from the BNC connectors on the top. When the top piece is placed on the mounting plate and secured with screws the spring loaded contacts rests on the copper ribbons and provide the electrical connections necessary.

A five-stage voltage supply was built from five EMCO model C30N miniature high voltage supplies to replace the single-stage supply used in the single stage experiments. Each of the miniature supplies would take an input and multiply it by a factor of 625. The five supplies were mounted into one box with five input lines, five output lines and a single common ground. An image of the five-stage power supply is shown in Figure 4.9.

In order to drive the five-stage high voltage supply a *National Instruments*, model BNC-2100, eight channel analog output device seen in Figure 4.10 was acquired. It came with a data acquisition (DAQ) card to allow computer control. Two main LabVIEW programs were created to control the analog output device.

The first LabVIEW program was used to create a driving function that caused the beam deflector to scan through the range of voltages set by the operator. The parameters available to the operator are listed in Table 4.2.

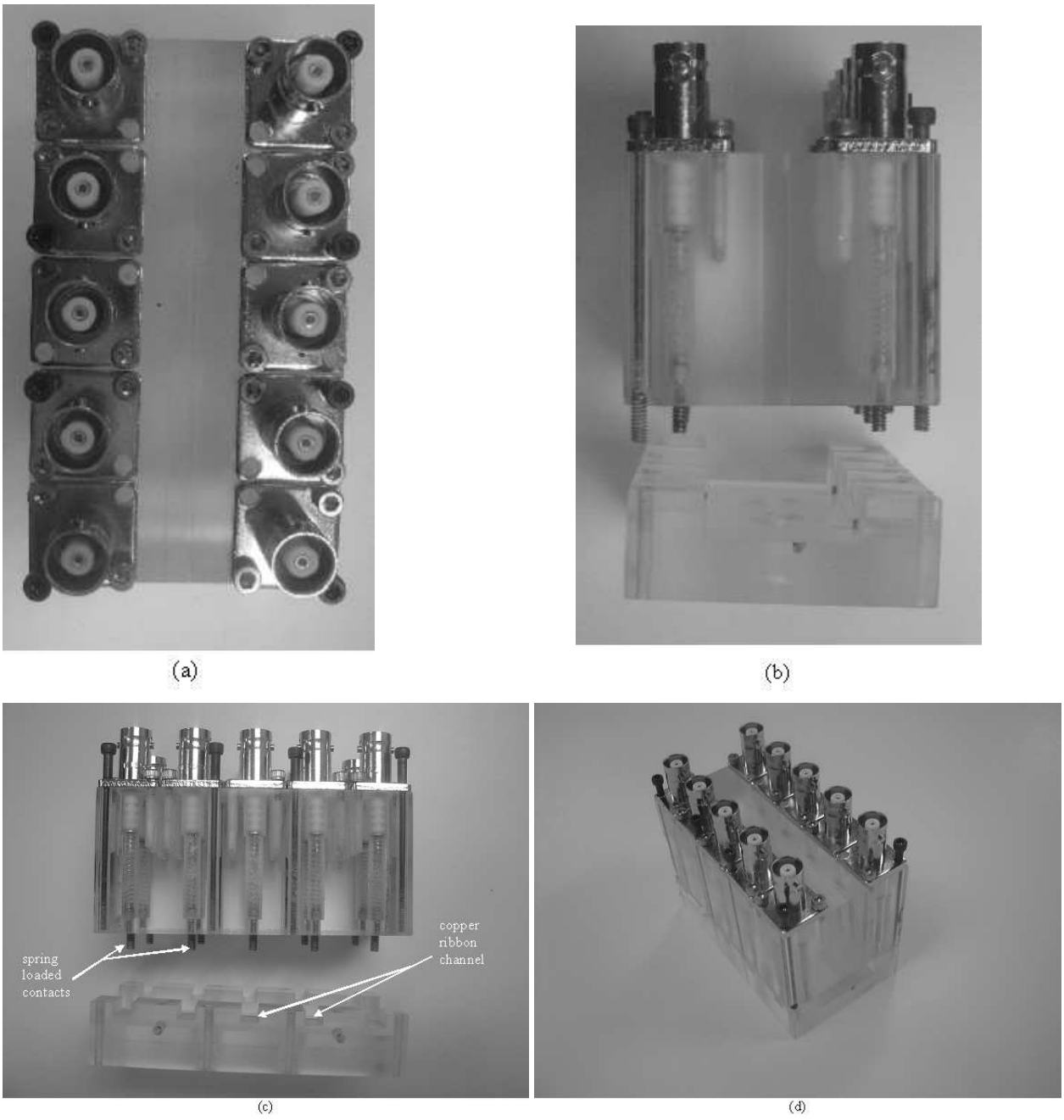

Figure 4.8: Five-stage mount. (a) top view with the high-voltage coaxial connections visible, (b) end view with the recess in the device mounting plate visible, (c) side view with the ribbon channels and the spring loaded contacts visible, (d) angle view of the top and bottom pieces connected.

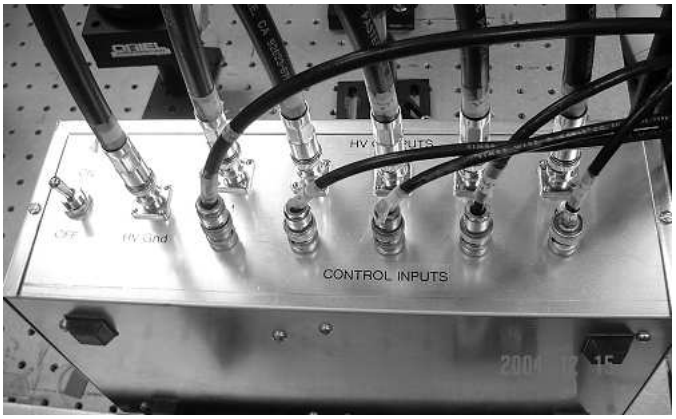

Figure 4.9: Five-stage high-voltage power supply

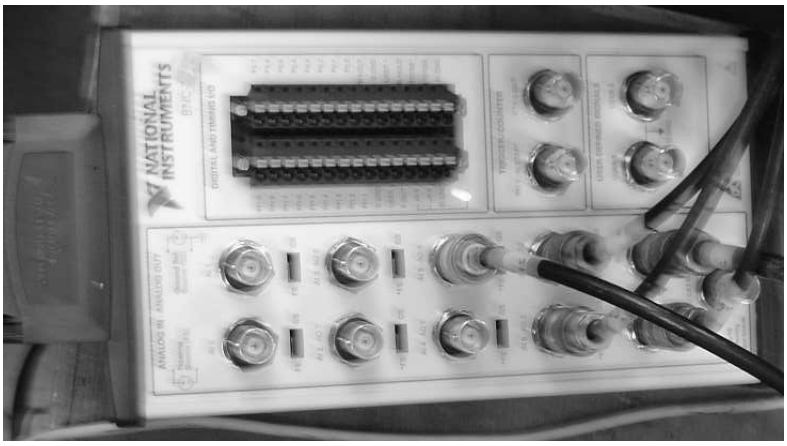

Figure 4.10: National Instruments analog output device

Table 4.2: Parameters for function generator LabVIEW program.

Parameter	Value Range	Note
Function type	Triangle Sine Sawtooth Square	Default - triangle wave
Maximum voltage	0 - 1.8 (kV)	Default - 1.4
# of stages	0 - 5	Number of stages driven by function
Hold Stages	0 - 5	Number of stages to hold at max voltage.
Duty Cycle	0 - 100%	Square wave only
Frequency	0 - 10GHz	Actual frequency is limited by supplies not by the program

The function generator program creates five synchronized voltage signals from a single function. For multi-stage operation the device stages must be driven by a set of voltages that are coordinated so that higher stages are not turned on until the lower stages have reached maximum steering voltage. This prevents later stages from contributing to steering before the beam is fully aligned by steering in previous stages. For example, the triangle wave function has stage 1 ramp from zero to the maximum voltage and hold. At the point that stage 1 reaches the maximum voltage, stage two begins ramping up to the maximum voltage and then it holds while the subsequent stages ramp up as well. This repeats for all stages up to the number set in a '# of stages' program parameter. Then there is a synchronized ramp down. Figure 4.11 shows a screen shot of the program driving five stages with a triangle wave and a maximum voltage of 1.4 kV for each stage.

This program was useful in the alignment process. The device alignment was adjustable by elevation, tilt, yaw, direction and position. The device was first aligned with no applied voltage to achieve a clean set of beams with no reflected modes off the top/bottom or the sides of the device. Reflections off the top or bottom resulted in additional rows of beamlets below or above the main set of beams or the beams would diverge upward or downward from the unreflected path. Side reflections caused some or all of the beams to be deflected to the right or left.

However, a clean set of beams did not guarantee good alignment. The beams could pass through the device without properly entering a channel. Also, when no voltage is applied to the device there is theoretically no index difference through device crystal. Although disturbances in the beamlet structure suggested the presence of an index gradient at zero bias, it was not usually possible to have the beams well aligned without having applied voltage to verify the device was properly steering the beams.

The function generator program was used to create a slowly varying voltage signal to drive the device to aid in alignment. As the voltage on a particular stage increased, any divergence from the expected deflection path could be noted and cor-

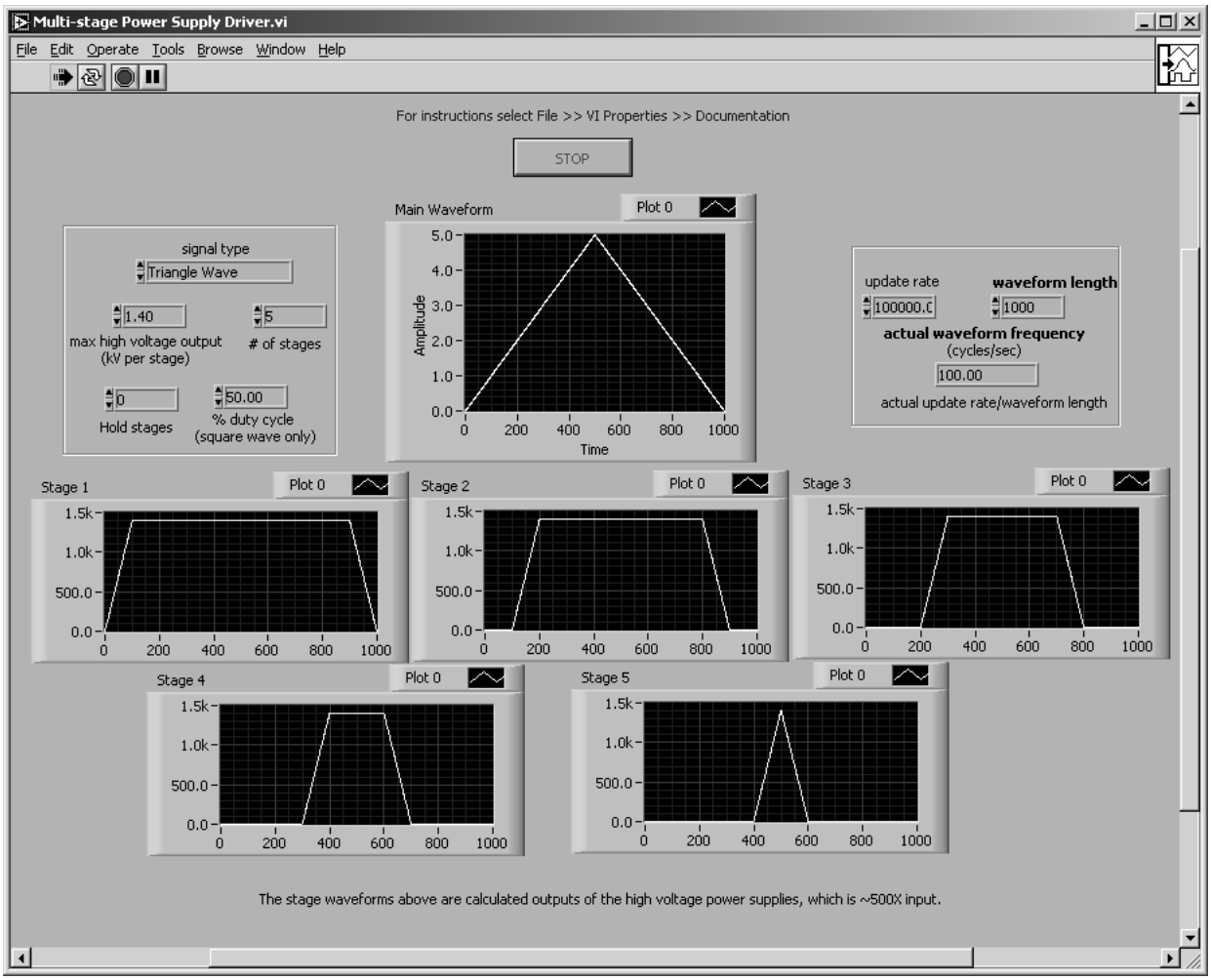

Figure 4.11: Multi-stage function generator configured for a five-stage triangle wave with 1.4 kV max voltage.

rected by tweaking the alignment. The program could be configured to drive multiple stages. It could also be set to hold some of the driven stages at maximum voltage and only vary the higher stages. Alignment was best performed one stage at a time. The holding configuration allowed for alignment to be adjusted in one stage at a time to find the best overall device position. Figure 4.12 shows a screen shot of the program driving five stages with a triangle wave, and holding the first two stages at the maximum voltage of 1.4 kV.

The diagram of the main LabVIEW program and the primary subprogram are shown in Figures 4.13 and 4.14. The main flow of the program is from left to right.

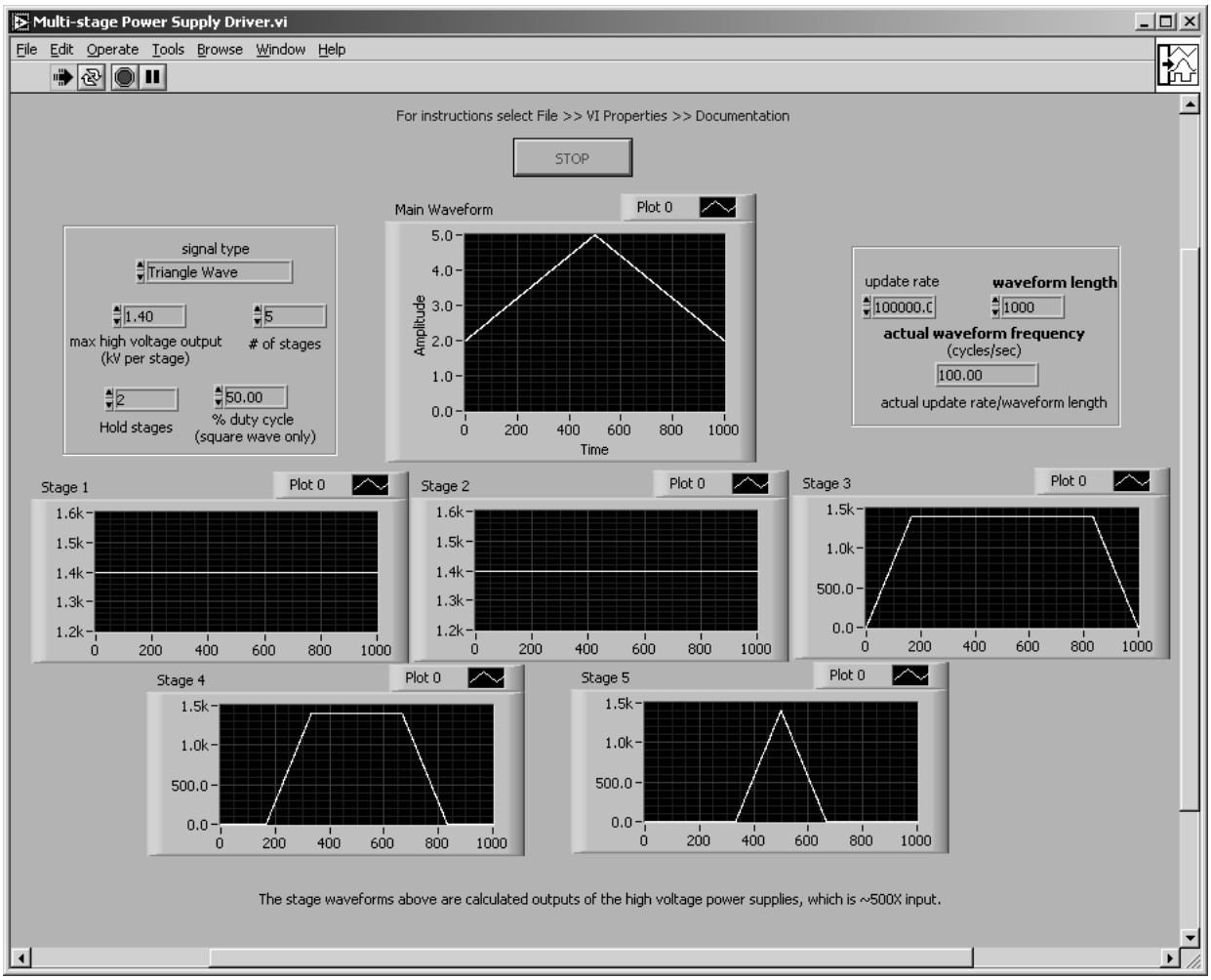

Figure 4.12: Multi-stage function generator configured for a five-stage triangle wave holding stages 1 and 2 with 1.4 kV max voltage.

Outside of the main box is an initialization routine on the left and some error checking and resets for program termination on the right. Inside the main box on the left are the inputs as listed in Table 4.2. Then the inputs are connected to a conditional box that checks for changes to the inputs. When there are changes the program re-initializes the waveform. Once the waveform is generated by the subprogram, indicated in the Figure, it is sent to the analog output programs and to the control panel display.

The waveform generator, in Figure 4.14, generates the basic waveforms in the lower left part of the screen shot. The amplitude of the basic wave is one. Then the waveform is multiplied by the number of stages to drive and a dc component added

with some conditional logic in the upper left portion of the diagram. The waveform at this stage has a peak amplitude equal to the number of stages to be driven and a dc value equal to the number of stages to be held at peak as in Figure 4.15. Finally, the waveform is used to create five separate waveforms. The stage one waveform is equal to the altered waveform for values between zero and one. For stage two, the waveform is altered further by subtracting one from it and then the stage two waveform takes on the values of the waveform between zero and one. Once all the stages are created they are all multiplied by the max output voltage.

Once the device was aligned, data had to be collected. The function generator was not convenient for data collection. A different LabVIEW program was created to allow individual control at constant voltage levels for each stage. Figure 4.16 shows a screen shot of this program. This multi-stage voltage controller program shown in Figure 4.17 is based off the same structure as the function generator. However, the inputs for this program are the individual voltage levels for the five stages. The 'waveform generator' was greatly simplified and merely creates a dc signal based off the square wave at 100% duty cycle.

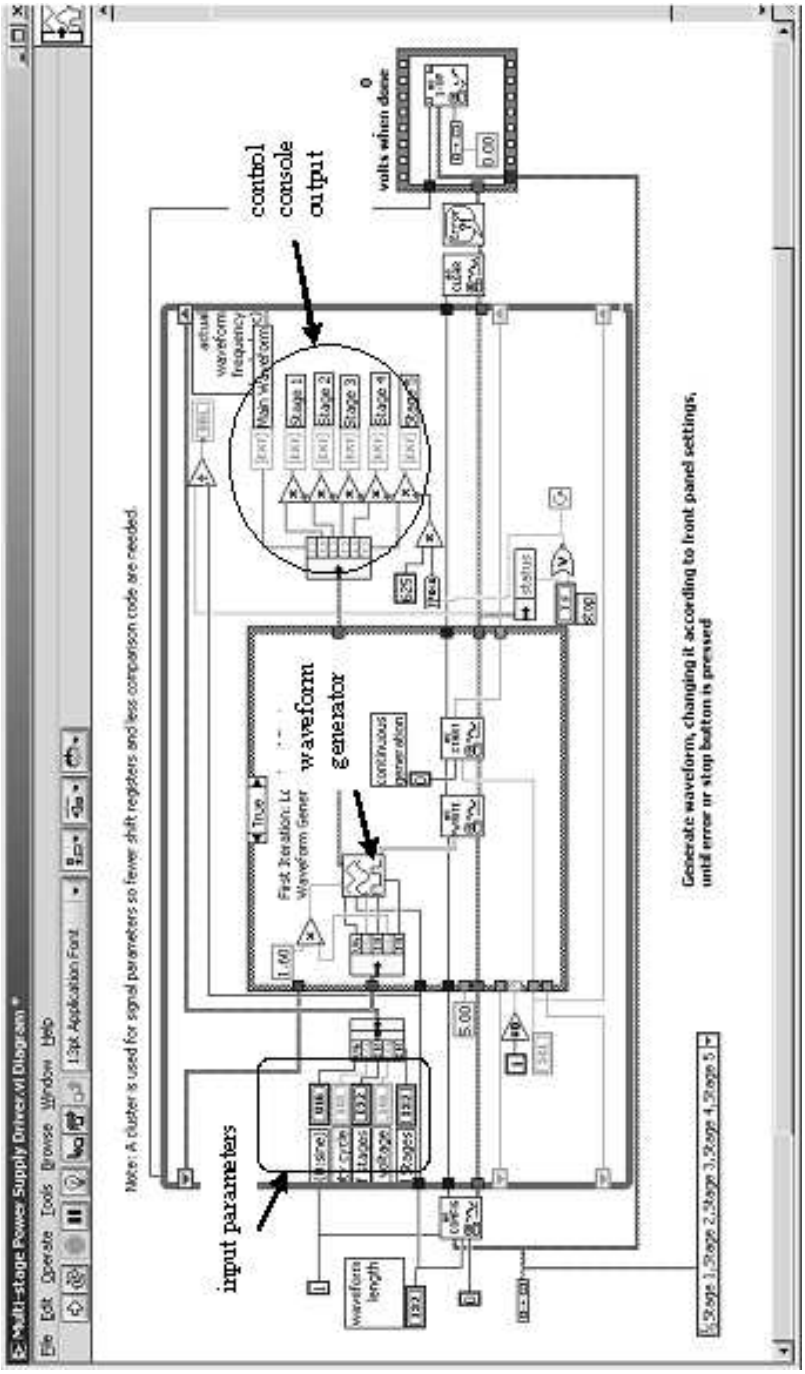

Figure 4.13: Diagram of the LabVIEW program for multi-stage function generator.

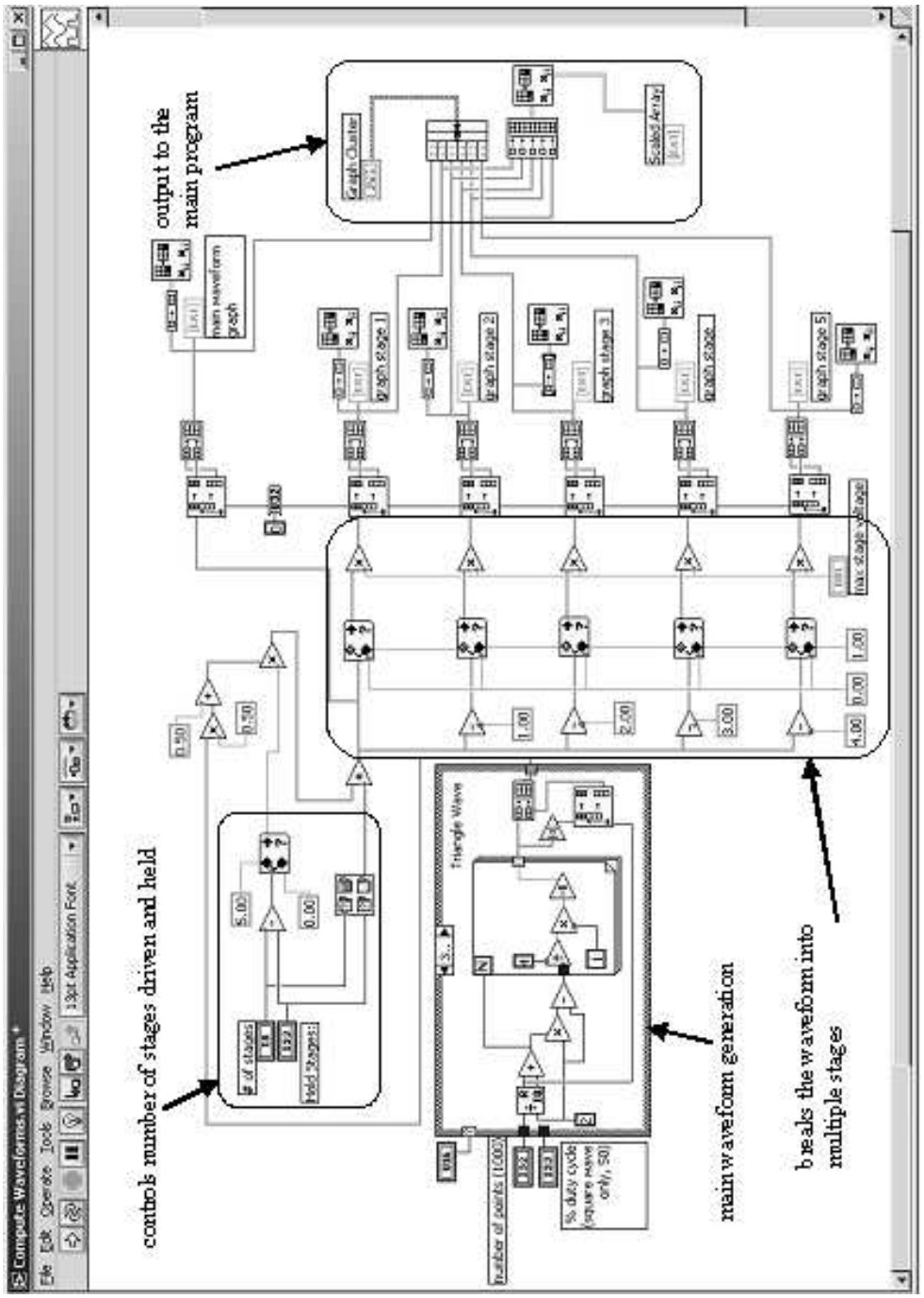

Figure 4.14: Diagram of the LabVIEW subprogram for waveform generation.

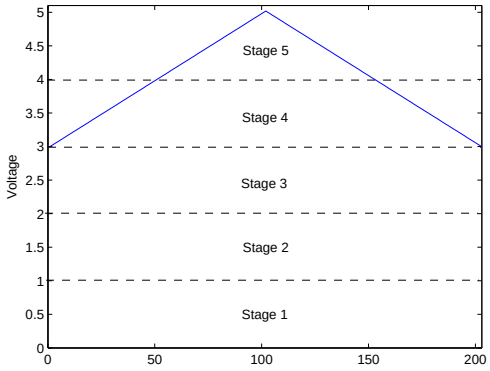

Figure 4.15: An illustration of the function generator waveform with the number of stages set to five and the number of held stages equal to three. The voltage level indicated is a intermediate value that is later scaled before output.

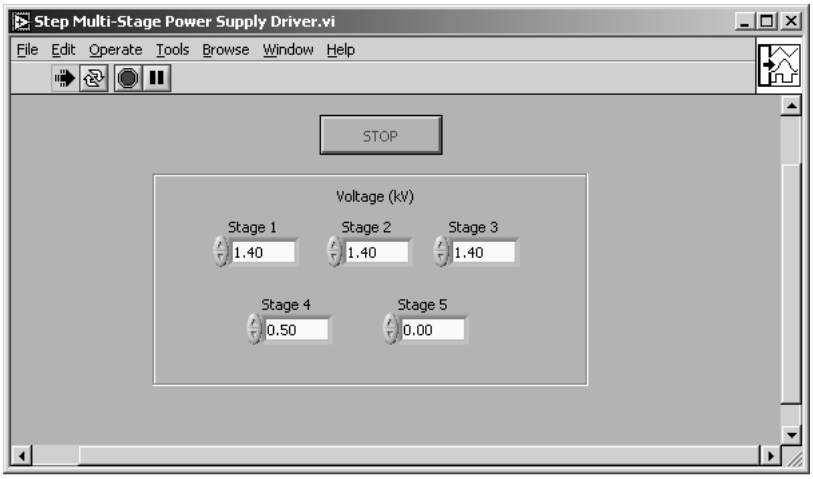

Figure 4.16: Multi-stage voltage controller driving stages 1-3 with 1.4 kV, stage four at .5 kV and stage five at zero.

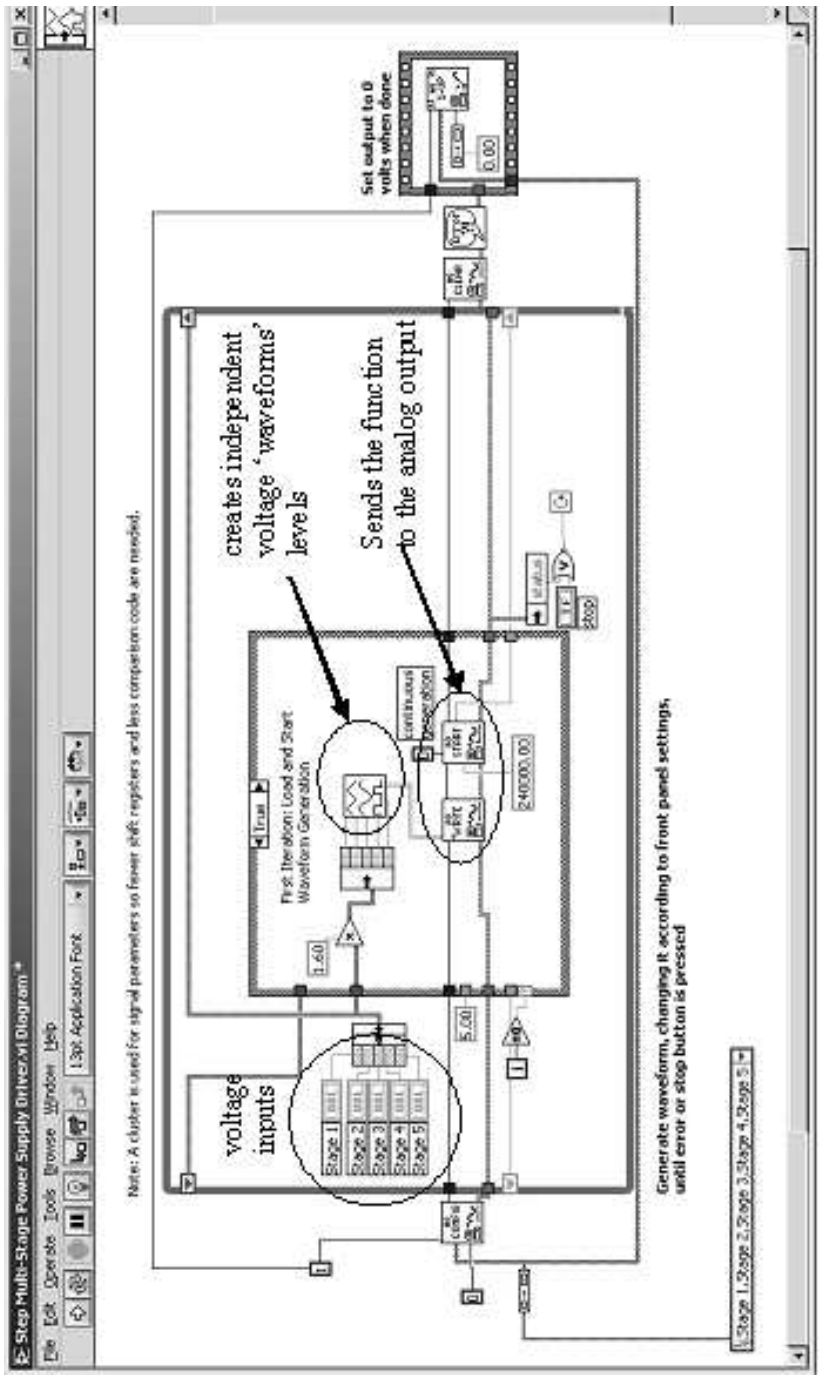

Figure 4.17: Diagram of the LabVIEW subprogram for the multi-stage voltage controller.

V. Experimental Results

5.1 Introduction

Results from the beam deflection experiment are presented with a discussion of the operation of the two devices. Next, the coupling experiment is addressed including a brief description of the attempts to improve the coupling efficiency. Finally, the far-field measurements are included.

5.2 Beam Deflection

The distance between the measurement planes (planes A and B as described in Figure 4.6) was 29.5 cm for the data reported in this section. The beam deflection was measured as described in Chapter IV to have a total deflection of 10.1° at a maximum applied voltage of 1.43 kV. However, the data presented below is steered with a maximum of 1.4 kV on each stage. This is slightly less than the designed maximum voltage. Therefore, the deflection angles in the figures below are slightly less than they would be if the device had been driven at the designed max. Previous work [19] shows that the device can also be operated at higher than the designed voltage levels, within limits, and achieve larger angles. The deflection angle for a given applied voltage can be found by using Equation 2.36

When investigation into the multi-stage operation of device one began, bleed-over between stage two and three was discovered. With 1.4 kV applied to the first stage, the bleed-over voltage at stage two was 800+ volts. In an attempt to discover the cause of the bleed-over the device was tested for ohmic connections between the two stages. The Fluke multi-meter used for this measurement did not reveal a short between the two stages. The bleed-over was unstable and only seemed to occur at high voltage.

It was found that the packaging of the device caused the copper ribbons for stages two and three to be close together when placed in the device mount. The bleed-over was significantly reduced by altering the packaging so the ribbons had a greater separation between them. This was accomplished by trimming some of the

rubber casing off the two ribbons which allowed for more flexible placement of the copper leads. The maximum bleed-over voltage dropped to ∼100 (± 25) volts.

As can be seen in Figure 5.1 the measured deflection angle closely matches theory except for the upper half region of stage 2 and a lower portion of the stage three region. Divergence from theory in this manner is explained by the bleed-over problem. Bleed-over into stage three at higher stage two voltage levels causes early beam deflection by stage three. When the applied stage three voltage overcomes bleed-over the deflection angle again matches theory.

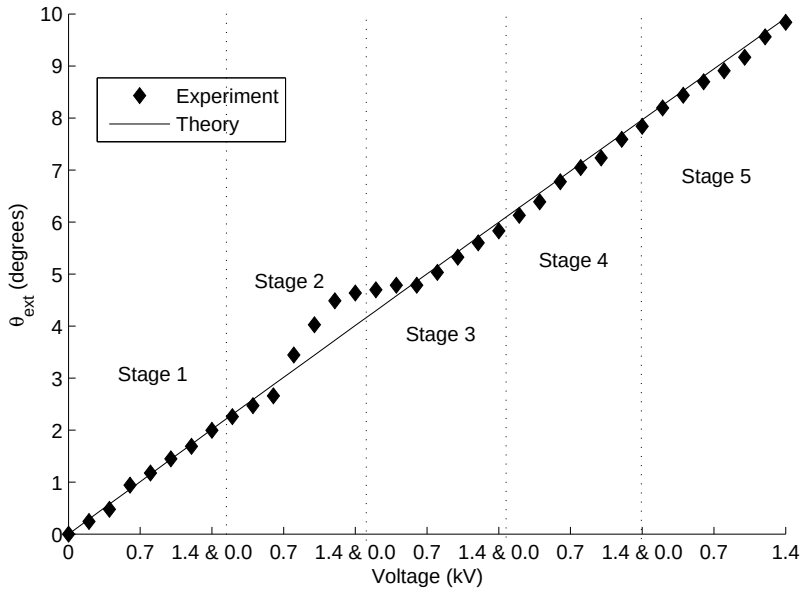

Figure 5.1: Device one deflection angle versus applied voltage across all stages.

Device two as mentioned earlier in Chapter IV, had stages four and five electrically shorted. These two stages could not be independently controlled. Additionally, a bleed-over problem from stage three to stage four/five was discovered on this device while recording deflection measurements. The device was mounted with the copper ribbons for stages one through three positioned in their respective ribbon channels on the device mount. The ribbons for stages four and five were both positioned in the same channel since they are shorted and would be at the same potential. In this configuration, the measurements for stage three deflection were very unstable and larger

than expected. It was then discovered that stage four/five had a bleed-over voltage present. When stage three was set at 1.4 kV stage four/five had a bleed-over voltage between 100-700 V. It was quite unstable and made it difficult to take consistent data for stage three deflection. The rubber casing was trimmed similar to the corrective step taken for the bleed-over problem of device one. In this case it did not reduce the bleed-over voltage.

To stabilize the stage three measurements the copper leads for stage four/five were tied to ground by placing them in the ribbon channel for the common ground connection. This allowed for the measuring of the deflection through stage three. Then the ribbons for stage four/five were replaced to their proper ribbon channel to allow them to have a steering voltage applied and stage four/five deflection angles were recorded. The deflection angle for low stage four/five voltages was expected to be unstable and almost meaningless. Voltages close to maximum were expected to produce deflection very near the theoretical max for a properly packaged five-stage device. At maximum voltage, the bleed-over problem would be overcome and all five stages would be at maximum deflection. Figure 5.2 shows the deflection plot for device two.

The theoretical plot has been altered to reflect the shorted stage configuration. The dashed line shows the theoretical angle for deflecting through the stage four range as if no short existed to stage five. The solid line in the stage four/five region of the graph shows the theoretical angle when deflecting through the stage five range as when no short exists with stage four. As seen in the figure, stage one through three closely follows theory. At low stage four/five voltages the angle is unstable but remarkably follows stage four theory. Then at $\sim$1.0 kV, the angle jumps to closely match the stage five theory. This occurs once the total deflection angle aligns the beams within the channels well enough to have both stage four and five steering.

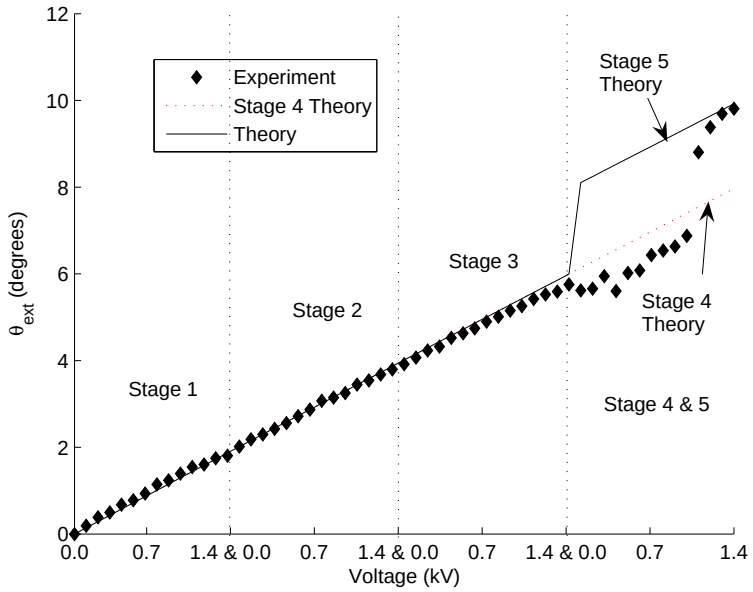

Figure 5.2: Device two deflection angle versus applied voltage across all stages.

5.3 Coupling

The predicted coupling efficiency can be found by considering the Fresnel losses at the entrance and exit faces of the device. No anti-reflection coating was on the faces of the device so the reflectance, R, is found from

$$R = \left(\frac{1 - n_e}{1 + n_e}\right)^2 . \tag{5.1}$$

For a refractive index of 2.1403, there is a Fresnel loss of 13.2% at each face. The theoretical transmission coupling efficiency, η_c^{ideal}, is found to be 75.4% using

$$\eta_c^{ideal} = (1 - R)^2 . \tag{5.2}$$

The measured coupling efficiency for the device one was previously reported [19] to be greater than 71% with no steering voltage applied. This represents only a 5% loss of signal when Fresnel losses are accounted for. The current study initially only yielded efficiencies around 50.6%. This was improved to about 60% by exchanging

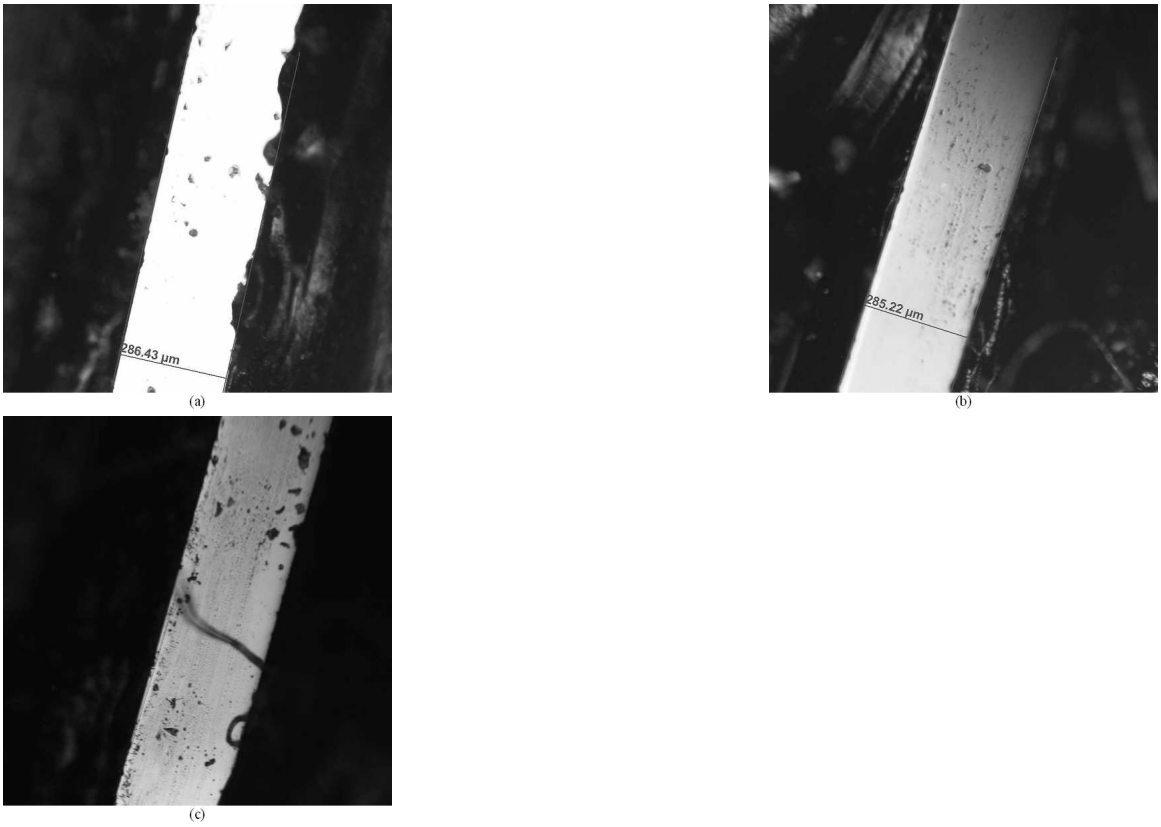

Figure 5.3: Device 2 edge (a) Indicates a thickness of ∼286 μm. There are also some pits in the device surface and some minor packaging materials obstructing the edges of the surface, (b) Indicates a thickness of ∼285 μm. There are some pits in the surface but this region is relatively free of other obstructions. (c) Some packaging material obstructing part of the surface.

the vertical focusing lens with a softer focus lens, changing the device placement and improving alignment.

The device edge was observed with a microscope to verify the thickness to be ∼286 μm and to observe the surface condition of the devices. Sample images are shown in Figure 5.3. Some imperfections on the device edges were observed, including pits in the surface and materials which were likely artifacts from the packaging process. These obstructions were not deemed significant enough to lower the expected coupling efficiency.

Beam size measurements were made at various points in the beam path with the device removed. It was discovered that the device was placed at a location where the

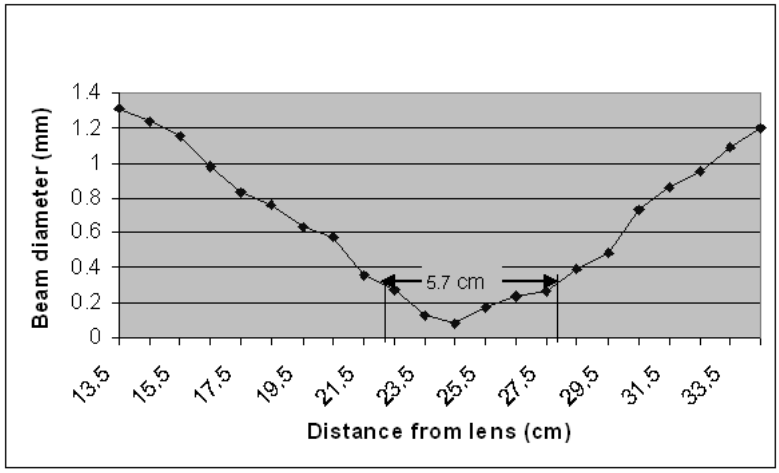

Figure 5.4: Beam size as it propagates after new lens with a focal length of 20 cm in air only.

beam diameter in the vertical direction was larger than the device thickness measured to be approximately 286 μm. Additionally, the beam was found to diverge too rapidly in the vertical direction to remain confined in the device for the entire device length of 5.5 cm. The vertically focusing cylindrical lens in Figure 4.4 with a focal length of 10 cm, was replaced with a lens with a focal length of 20 cm. With the new lens in place and the device removed the beam diameter was measured to be less than the device thickness for a total length of 5.7 cm as shown in Figure 5.4. Gaussian beam propagation calculations as shown below reveal that the beam focus is further softened by the interface with the device. This increases the total propagation distance for which the beam fits in the device to $\sim$8 cm.

Standard Gaussian beam propagation can be calculated by evaluating the following matrix expression

$$\begin{bmatrix} 1 & z_2 \\ 0 & 1 \end{bmatrix} \begin{bmatrix} 1 & 0 \\ 0 & \frac{1}{n_e} \end{bmatrix} \begin{bmatrix} 1 & z_1 \\ 0 & 1 \end{bmatrix} \tag{5.3}$$

where z_1 and z_2 are the propagation distances before and after the interface. The matrix on the right represents the propagation of the beam waist to the interface. In this case the free-space beam waist is virtual because the device is placed such

that the beam waist is after the interface to which it is propagating. Therefore the propagation distance, z_1, is negative. The middle matrix represents the interface, while the matrix on the left represents the propagation of the beam waist after the interface. The result of the expression in Equation 5.3

$$\begin{bmatrix} 1 & z_1 + \frac{z_2}{n_e} \\ 0 & \frac{1}{n_e} \end{bmatrix} \tag{5.4}$$

The final results can be found by evaluating the following

$$q_2 = \frac{Aq_1 + B}{Cq_1 + d} \tag{5.5}$$

where A, B, C and D are the standard matrix elements for the matrix in Equation 5.4. When the device is placed such that the free-space beam waist is 2.5 cm inside the device (i.e., z_1 = -2.5 cm), the new beam waist is calculated to be past the exit face of the device at ∼8cm from the entrance face. This calculation did not include the effect of the exit interface. However, it sufficiently demonstrates that the beam will be confined within the device for the entire length of the device.

After the above changes and with improved alignment, the coupling efficiency was increased to 59.7% for device one and 61.6% for device two. Although this is still smaller than the 71% reported earlier no additional increases could be obtained by further adjusting alignment of the device. Sample data for these measurements are presented in Table 5.1.

Table 5.1: Sample coupling data for both devices.

Device	P_{in} (mW)	P_{out} (mW)	η_c
1	1.49	0.89	59.7%
2	1.25	0.77	61.6%

5.4 Far-Field Pattern

The intensity pattern of the beams in the far-field are well predicted by calculating a many-slit diffraction pattern. The lens array produces a far-field pattern similar to that of a 14 slit aperture with slit spacing, a, of 500μm and slit size, b, of 300μm. This is calculated by the following equation,

$$I(\theta) \propto \left(\frac{\sin(\beta)}{\beta}\right)^2 \left(\frac{\sin(N\alpha)}{\sin(\alpha)}\right)^2. \tag{5.6}$$

where $\beta = (kb/2)\sin(\theta)$, $\alpha = (ka/2)\sin(\theta)$ and N is the number of slits. The pattern is displayed in Figure 5.5 where θ is in radians and the intensity is in arbitrary units. As a point of comparison a cross-section of the intensity of an experimental far-field image is shown in Figure 5.6

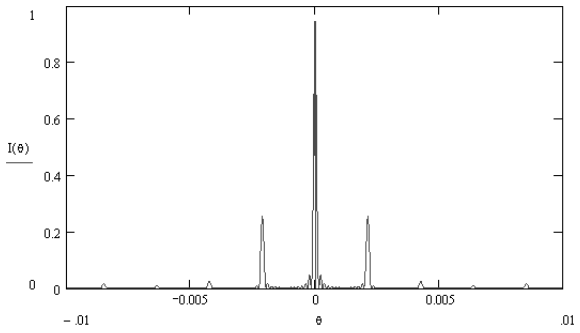

Figure 5.5: Calculated cross-section of the far-field intensity pattern of 1.064 μm light diffracted through 14 slits with slit spacing of 500 μm and slit size of 300 μm.

The mode angles in this plot obey the grating equation below

$$a\sin(\theta_m) = m\lambda. \tag{5.7}$$

where $m = \pm 1, \pm 2, \ldots$. If we assume that applying a steering voltage is equivalent to modifying the blaze angle of a diffraction grating then that suggests the steering angle would have possible discrete values that are determined by Equation 5.7. In fact this seems to be the case. See the set of far-field images in Figure 5.7. The figure shows the image scanned through the first stage range. Notice light is never deflected

into the nulls as the beam is scanned across. A possible solution is described in the next chapter.

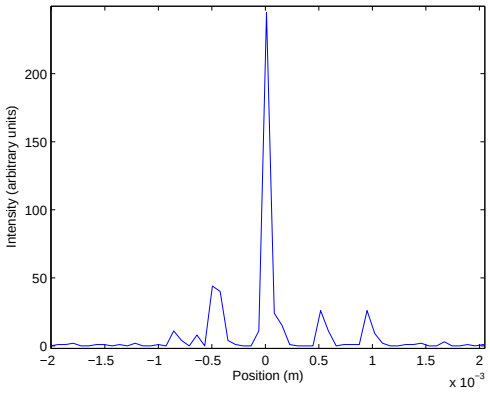

Figure 5.6: Cross-section of the far-field intensity image of the 1.064 μm light through device one at zero bias.

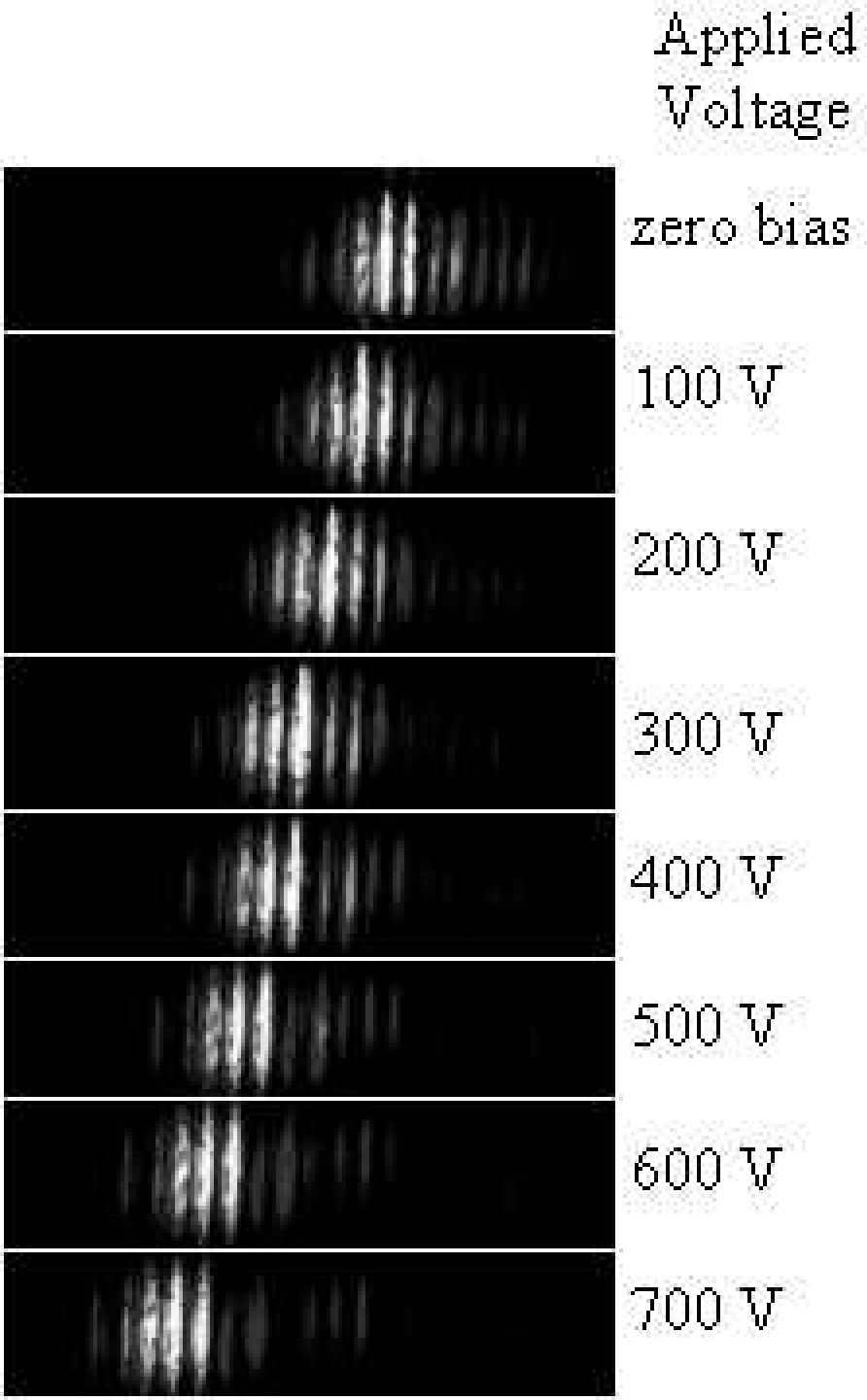

Figure 5.7: Far-field intensity images of the 1.064μm light with a range of driving voltages on the first stage of device one.

VI. Conclusions

6.1 Summary

This thesis focused on the characterization of a 14-channel five-stage electro-optic beam-steering device from micro-domain engineered $LiTaO_3$. The device deflection angle agreed well with theory. The maximum steering angle at 1.43 kV for both devices was 10.1° while the expected angle was 10.3°. The experimental results are within 0.3% of the designed maximum angle. Further beam deflection should be achievable by adding additional stages to the device design. Additional work for this research included the development of control equipment and the exploration of in-house fabrication techniques.

The theory of device design and operation was explained in Chapter 2. Typical prism scanners, upon which this design is based, have a trade off between beam size and maximum scanning angle. This device utilizes shape optimization based on a horn shaped scanner discussed in Chapter II and uses multiple channels to allow for both large diameter beams and large deflection angles.

Local microelectronics clean-rooms and poling equipment were used to attempt the fabrication of additional devices. The procedures were adapted from previous local micro-domain engineering work [20] and from the fabrication work for the two devices provided by PSU [17].

The maximum measured coupling efficiency of the beam steering devices was 59.7% for device one and 61.6% for device two. Although this efficiency was low compared to the theory of 75% based on Fresnel losses devices and even compared to previous measurements [19], it is high compared to other non-inertial steering systems such as a liquid crystal device [14]. Although substantial effort was made, this experiment failed to produce the same efficiency as in previous measurements.

6.2 Recommendations

There are several areas to be explored in later related research work. The present work has demonstrated the operation through all five stages of the multi-channel

device. Here we have scanned a single row of beamlets in a single device. However, ultimately, it is desirable that the device be able to deflect a two-dimensional beam. For this, several identical devices must be stacked and aligned to couple in multiple rows of beamlets. The current device mount should allow for this type of experiment, however it may need modification to expand the device mounting area.

Additionally, the far-field analysis revealed a multi-slit pattern that had forbidden steering angles. A possible solution to overcome the forbidden angles an electro-optically induced relative phase delay might be introduced in each channel path. This method would require an additional cable for every channel in the device. Currently all channels are designed to have equal phase. However, by integrating a set of phase delay channels that are individually and electro-optically controlled, a relative phase difference could be introduced between adjacent channels. The relative phase delay might be controlled such that instead of shifting the energy from one mode to the next as the current design does, the location of the central mode itself might be shifted. Similar work has been reported elsewhere [13].

For a system that has a dual polarity voltage supply the maximum relative phase delay necessary would be $\pm\pi$. The maximum delay would result in a n optical path length difference of $\lambda/2$ at the exit of the phase delay channels. For light polarized in the z direction, a channel with zero bias has an optical path length of $n_e d$, where d is the physical length of the channel. When a bias is applied the optical path length becomes

$$(n_e + \Delta n_e)d = n_e d + \Delta n_e d. \tag{6.1}$$

where Δn_e is the electro-optically induced change in the index. Combining with Equation 2.32

$$\Delta n_e d = \pm\frac{1}{2} n_e^3 r_{33} E d. \tag{6.2}$$

For the maximum phase difference $\Delta n_e d = \frac{\lambda}{2}$. When the phase delay channel length, $d = .5cm$, a device thickness, $t = .5mm$, $n_e = 2.1403$, and $r_{33} = 29.14 \times 10^{-12}$ the

voltage necessary to achieve the maximum phase delay is found thus,

$$V = \pm \frac{\lambda t d}{n_e^3 r_{33}} \approx 370V. \tag{6.3}$$

To determine the amount of phase shift necessary to achieve a particular angle we use the following equation adapted from [10]

$$W \sin(\theta_m) = m\lambda \pm \Delta n_e d. \tag{6.4}$$

where W is the distance between channels, θ_m is the angle of the mth order of the far-field pattern. Combined with Equation 6.2 and when $m = 0$ the expression becomes

$$\frac{1}{2} n_e^3 r_{33} E d = W \sin(\theta_m). \tag{6.5}$$

For example, Figure 5.5 reveals that a forbidden angle exists at ∼0.9 mrad. In order to steer into that angle, a relative path length difference, from Equation 6.4, is .55 μm. The voltage necessary to achieve this angle can be found from Equation 6.6 to be

$$V = \frac{2W \sin(\theta_m) t}{n_e^3 r_{33} d} \approx 316V. \tag{6.6}$$

Design and fabrication of a new device that implements the multi-channel relative phase control is recommended. This new experiment will not only require the design and fabrication of the device itself, but also the creation of new control equipment because the new device will have a separate voltage lead to each channel in addition to the voltage leads for the individual stages. Although this configuration may have promise, the requirement of additional cables may render this concept impractical. The six connections that were necessary in the design implemented in this research was quite cumbersome and the addition of 14 more cables would have made device alignment even more difficult to maintain.

Even without the development of the new design, the fabrication of additional devices should be explored. The current devices have certain defects affecting operation, such as the short between stages four and five on device two, and the bleed-over problem on both devices. However, it appears that the defects were introduced during the packaging and are not inherent in the device. The only way to be sure is to produce additional devices and find procedures that will eliminate defects as much as possible.

Finally, as a practical matter, for any follow-on efforts, an upgrade to the five-stage high-voltage supplies used for this experiment is suggested in order to increase switching frequency. Although, the system was sufficient for this effort, the supplies were slow ($\sim$1 Hz) which made them sometimes cumbersome and a nuisance for certain aspects of the alignment process.

Bibliography

1. Barrington, Stephen J., Alexander J. Boyland, and Robert W. Eason. "Domain-Engineered Lithium Niobate as a Medium for an Integrated Solid-State Two-Dimensional Color Laser Scanning System". *Applied Optics*, 43(8):1625–1627, March 2004.

2. Boyd, Robert W. *Nonlinear Optics*. Academic Press, 525 B Street, Suite 1900, San Dieago, CA 92191-4495, second edition, 2003.

3. Burns, David M. *Microelectromechanical Optical Beam Steering Systems*. Ph.D. thesis, Air Force Institute of Technology, December 1997.

4. Chen, Q. et al. "Guided-wave electro-optic beam deflector using domain reversal in $LiTaO_3$". *Journal of Lightwave Technology*, 12:1401–1404, August 1994.

5. Chiu, Yi et al. "Shape-Optimized Electrooptic Beam Scanners: Analysis, Design, and Simulation". *Journal of Lightwave Technology,*, 17(1):108–114, January 1999.

6. Coppola, Giuseppe et al. "Visualization of Optical Deflection and Switching Operations by a Domain-Engineered-Based $LiNbO_3$". *Optics Express*, 11(10):1212–1222, May 2003.

7. Gahagan, Kevin T. et al. "Integrated high-power electro-optic lens and large-angle deflector". *Applied Optics*, 40(31):5638–5642, November 2001.

8. Gervis, Francois and Vicente Fonseca. *Handbook of Optical Constants of Solids*, volume 3, chapter Lithium Tantalate, 777–805. Academic Press, San Diego, CA, 1998.

9. Goodman, Joseph W. *Introduction to Fourier Optics*. McGraw-Hill, New York, NY, second edition, 1996.

10. Hecht, Eugene. *Optics*. Addison Wesley, San Fransisco, CA, fourth edition, 2002.

11. Lotspeich, J. F. "Electrooptic light-beam deflection". *IEEE Spectrum*, 45–52, February 1968.

12. Marshall, Gerald F. *Optical Scanning*. Optical Engineering. Marcel Dekker, Inc., 270 Madison Ave, New York, NY 10016, 1991.

13. Meyer, R.A. "Optical Beam Steering Using a Multichannel Lithium Tantalate Crystal". *Applied Optics*, 11(3):613–616, March 1972.

14. Miani, Lino M. *Theory and Analysis of a Liqiud Crystal Beam Steering Device*. Master's thesis, Air Force Institute of Technology, December 1990.

15. Muhammad, Fikri et al. "Multichannel 1.1-kV Arbitrary Waveform Generator for Beam Steering Using Ferroelectric Device". *IEEE Photonics Technology Letters*, 14(11):1605–1607, November 2002.

16. Nakamura, Masaru et al. "Refractive Indices in Undoped and MgO-Doped Near-Stoichiometric $LiTaO_3$ Crystals". *Japanese Journal of Applied Physics*, Part 2 41:L465–L467, February 2002.

17. Scrymgeour, David A. et al. "Large-angle Electro-Optic Laser Scanner on $LiTaO_3$ Fabricated by in Situ Monitoring of Ferroelectric-Domain Micropatterning". *Applied Optics*, 40(34):6236–6241, December 2001.

18. Scrymgeour, David A. et al. "Cascaded Electro-Optic Scanning of Laser Light Over Large Angles". *Applied Physics Letters*, 81(17):3140–3142, October 2002.

19. Scrymgeour, David A. et al. "Phased Array Electro-Optic Steering of Large Aperture Laser Beams Using Microstructured Ferroelectrics", 2005.

20. Vershure, Eric. *Periodically Poled Crystals*. Master's thesis, University of Dayton, January 2005.

21. Yariv, Amnon and Pochi Yeh. *Optical Waves in Crystals: Propagation and Control of Laser Radiation*. Wiley Series in Pure and Applied Optics. John Wiley and Sons, New York, NY, 1984.

REPORT DOCUMENTATION PAGE

Form Approved
OMB No. 0704–0188

The public reporting burden for this collection of information is estimated to average 1 hour per response, including the time for reviewing instructions, searching existing data sources, gathering and maintaining the data needed, and completing and reviewing the collection of information. Send comments regarding this burden estimate or any other aspect of this collection of information, including suggestions for reducing this burden to Department of Defense, Washington Headquarters Services, Directorate for Information Operations and Reports (0704–0188), 1215 Jefferson Davis Highway, Suite 1204, Arlington, VA 22202–4302. Respondents should be aware that notwithstanding any other provision of law, no person shall be subject to any penalty for failing to comply with a collection of information if it does not display a currently valid OMB control number. **PLEASE DO NOT RETURN YOUR FORM TO THE ABOVE ADDRESS.**

1. REPORT DATE *(DD–MM–YYYY)*	2. REPORT TYPE	3. DATES COVERED *(From — To)*
21–03–2005	Master's Thesis	Jun 2004 — Mar 2005

4. TITLE AND SUBTITLE

Electro-optic beam steering using Domain Engineered Lithium Tantalate

5a. CONTRACT NUMBER

5b. GRANT NUMBER

5c. PROGRAM ELEMENT NUMBER

6. AUTHOR(S)

Daren J. Chauvin, Capt, USAF

5d. PROJECT NUMBER

5e. TASK NUMBER

5f. WORK UNIT NUMBER

7. PERFORMING ORGANIZATION NAME(S) AND ADDRESS(ES)

Air Force Institute of Technology
Graduate School of Engineering and Management
2950 Hobson Way
WPAFB OH 45433-7765

8. PERFORMING ORGANIZATION REPORT NUMBER

AFIT/GEO/ENP/05-01

9. SPONSORING / MONITORING AGENCY NAME(S) AND ADDRESS(ES)

AFRL/SNJW
Attn: Dr Kenneth L. Schepler
2241 Avionics Circle, Bldg 620
WPAFB, OH 45433-7318

10. SPONSOR/MONITOR'S ACRONYM(S)

11. SPONSOR/MONITOR'S REPORT NUMBER(S)

12. DISTRIBUTION / AVAILABILITY STATEMENT

Approval for public release; distribution is unlimited.

13. SUPPLEMENTARY NOTES

14. ABSTRACT The operation of a 14-channel five stage electro-optic beam steering device was studied. Beam deflection scanned from 0° to 10.1° was demonstrated. The maximum angle is within 0.3% of design. Many laser systems in operation today implement mechanical beam steering methods that are often expensive in terms of cost, weight and power. They are slow and subject to wear and vibration. A non-inertial beam scanning mechanism, such as one based on the device studied in this research could enhance the performance of these systems. The device studied here is fabricated in LiTaO3 using micro-patterned domain reversal. The 14 channels allow for steering large aperture beams while the five cascaded stages increase the total deflection angle. The steering mechanism is a series of prisms created through domain reversal with the index change across prism interfaces controlled electro-optically. The maximum coupling efficiency achieved was 61.6% for this device. Also, the far-field observations revealed a pattern consistent with a beam diffracted through a multi-slit aperture. Forbidden angles exist between modes caused by destructive interference regardless of the applied voltage. A discussion on a method to improve device design, which allows the forbidden angles, is presented.

15. SUBJECT TERMS

Beam Steering, Optical Scanning, Ferroelectric Domain Engineering, Directed Energy Systems, Beam Deflection, Infrared Scanning

16. SECURITY CLASSIFICATION OF:			17. LIMITATION OF ABSTRACT	18. NUMBER OF PAGES	19a. NAME OF RESPONSIBLE PERSON
a. REPORT	b. ABSTRACT	c. THIS PAGE			Thomas G. Alley, Lt Col, USAF (ENP)
U	U	U	UU	81	19b. TELEPHONE NUMBER *(include area code)* DSN 785-3636 x4649 thomas.alley@afit.edu